จุดเย็นผิดปกติในสนามรังสีคอสมิคพื้นหลังที่เกิดจากช่องว่างในจักรวาล

นายอนุตร สังฆะ

วิทยานิพนธ์นี้เป็นส่วนหนึ่งของการศึกษาตามหลักสูตรปริญญาวิทยาศาสตรมหาบัณฑิต
สาขาวิชาฟิสิกส์
มหาวิทยาลัยเทคโนโลยีสุรนารี
ปีการศึกษา 2559

CMB COLD SPOT ANOMALY FROM COSMIC VOIDS

Anut Sangka

A Thesis Submitted in Partial Fullfillment of the Requirements for the

Degree of Master in Physics

Suranaree University of Technology

Academic Year 2016

CMB COLD SPOT ANOMALY FROM COSMIC VOIDS

Suranaree University of Technology has approved this thesis submitted in partial fulfillment of the requirements for the Degree of Master.

Thesis Examining Committee

(Assistant Prof. Dr. Worawat Meevasana)
Chairperson

(Dr. Nuanwan Sanguansak)
Member (Thesis Advisor)

(Dr. Utane Sawangwit)
Member

(Dr. Teeraparb Chantavat)
Member

(Prof. Dr. Sukit Limpijumnong)
Vice Rector for Academic Affairs
and Innovation

(Prof. Dr. Santi Maensiri)
Dean of Institute of Science

อนุตร สังฆะ : จุดเย็นผิดปกติในสนามคอสมิคพื้นหลังอันเนื่องมาจากช่องว่างในจักรวาล
(CMB COLD SPOT ANOMALY FROM COSMIC VOIDS)
อ.ที่ปรึกษา: อาจารย์ ดร.นวลวรรณ สงวนศักดิ์, 90 หน้า

วิทยานิพนธ์ฉบับนี้ได้ศึกษาต้นกำเนิดของจุดเย็นผิดปกติคอสมิกไมโครเวฟพื้นหลังซึ่งถูกค้นพบครั้งแรกโดยดาวเทียมดับเบิลยูแม็ปและต่อมาได้รับการยืนยันจากการสังเกตการณ์ของดาวเทียมแพลงค์ จุดเย็นผิดปกตินี้มีขนาดรัศมีเชิงมุม 10 องศาและมีอุณหภูมิ ณ จุดศูนย์กลางต่ำกว่าอุณหภูมิเฉลี่ยของคอสมิกไมโครเวฟพื้นหลังอยู่ 150 ไมโครเคลวิน และสูงกว่าอย่างมีนัยสำคัญเมื่อเทียบกับค่าความผันผวนของอุณหภูมิคอสมิกไมโครเวฟพื้นหลังอยู่ 18 ไมโครเคลวิน ดังนั้นจึงทำให้จุดเย็นผิดปกตินี้เป็นหัวข้อที่น่าสนใจหัวข้อหนึ่งในการศึกษาจักรวาลวิทยาเชิงกายภาพ

ในวิทยานิพนธ์ได้ศึกษาจุดเย็นผิดปกติในแง่ความผันผวนของอุณหภมิคอสมิกไมโครเวฟพื้นหลังระดับทุติยภูมิโดยเฉพาะอย่างยิ่งในแง่ของปรากฏการณ์ปริพันธ์ซาช-วูฟ (ไอเอสดับเบิลยู) เนื่องจากช่องว่างในจักรวาลสามารถทำให้อุณหภูมิคอสมิกไมโครเวฟพื้นหลังลดลงได้ในทิศทางของการสังเกตการณ์ นอกจากนี้ยังได้ศึกษาผลกระทบเนื่องจากเลนส์ความโน้มถ่วงด้วย ซึ่งพบว่าผลจากเลนส์ความโน้มถ่วงมีค่าน้อยมากเมื่อเทียบกับผลที่ได้จากปรากฏการณ์ไอเอสดับเบิลยู

แบบจำลองของช่องว่างในจักรวาลที่ใช้ในการพิจารณาสำหรับงานวิจัยนี้มีด้วยกันสามแบบ คือ ช่องว่างในจักรวาลเดี่ยวแบบ ฮามอท-ซัดเติล และเวลเดนท์ (เอทชเอสดับเบิลยู) แบบจำลองแลมาแตร์-ทอยแมนบอร์นดิ (แอลทีบี) และแบบจำลองหลายช่องว่างในจักรวาล สำหรับแบบเดี่ยวเราพบว่าจะต้องการรัศมีที่ใหญ่กว่า 150 เมกะพาร์เซกจึงจะสามารถอธิบายผลจากการสังเกตการณ์ได้ ซึ่งตามทฤษฎีการก่อตัวของโครงสร้างขนาดใหญ่แบบมาตรฐานนั้นความน่าจะเป็นที่จะพบโครงสร้างขนาดดังกล่าวมีเพียง 10^{-17} เท่านั้น ในขณะที่แบบจำลองแบบหลายช่องว่างในจักรวาลต้องการการจัดเรียงตัวในแนวตั้งฉากกับทิศทางการสังเกตที่เฉพาะเจาะจงโดยมีการกระจายตัวของช่องว่างในจักรวาลแบบเกาส์ และต้องการจำนวนช่องว่างในจักรวาลเป็นจำนวนประมาณ 36 ล้านช่องว่าง คิดเป็น 7.6 เท่าของค่าที่ได้จากทฤษฎีมาตรฐาน

สาขาวิชาฟิสิกส์	ลายมือชื่อนักศึกษา______________________
ปีการศึกษา 2559	ลายมือชื่ออาจารย์ที่ปรึกษา__________________
	ลายมือชื่ออาจารย์ที่ปรึกษาร่วม_______________

ANUT SANGKA : CMB COLD SPOT ANOMALY FROM COSMIC VOIDS. THESIS ADVISOR : NAUNWAN SANGUANSAK, Ph.D. 90 P.

CMB/COSMIC VOIDS/ISW EFFECT

This thesis investigates the origin of the Cosmic Microwave Background (CMB) cold spot anomaly. It was first detected by Wilkinson Microwave Anisotropy Probe (WMAP) and it is recently confirmed by Planck. The large cold spot has the angular radius 10 degree on the sky. The peak of cold spot is approximately 150 μK colder than the average CMB temperature and significantly higher than the CMB fluctuations, RMS = 18 μK. This makes the cold spot anomaly one of the most interesting topics in physical cosmology.

In this thesis, we consider cold spot to be the secondary CMB temperature anisotropy, mainly caused by the Integrated Sachs-Wolfe (ISW) effect. The void ISW effect can lower the CMB temperature along its line of sight. In additions, we consider the weak gravitational lensing. Our study had shown that CMB weak lensing is insignificant when compare to ISW.

Three models of cosmic voids are considered in this work, namely, the single void models with Hamaus, Sutter and Wendelt (HSW) and Lemaître-Tolman-Bondi (LTB) profiles and the multi-void model of HSW profile. To explain the observed data, both single void models require a void with radius greater than 150 Mpc h^{-1} with equates to the existence probability 10^{-17} . For multi-void model, it requires alignment of voids that follow normal distribution perpendicular to the line of sight and requires approximately 36 millions voids , 7.6 times the standard model prediction.

School of Physics — Student's Signature ____________

Academic Year 2016 — Advisor's Signature ____________

Co-advisor's Signature ____________

ACKNOWLEDGEMENTS

I am grateful first and foremost to my supervisors, Dr.Nuanwan Sanguansak and Dr.Utane Sawangwit, for their support, time and guidance. This thesis would not have been possible without their supervision, enthusiasm and vast knowledge of cosmology and general astronomy.

I would like to thank the SUT's scholarship for outstanding student, Thailand Research Fund (TRF) under Grant No. IRG57800010 and National Astronomical Research Institute of Thailand (NARIT). And aslo Mrs. Phenkhae Petchmai who always works hard to systematise between me and the others. Without these supporters, this thesis could not be success.

I appreciate my friends in research group which includes Mr. Niwat Hemha, Mr. Kittipong Wangnok, Mr. Khunagron Chanthon Mr.Wanchaloem Kharmmai, Miss Jaruchit Siritpak, Mr. Raengboon Incee and Miss Rungtiwa Khawram. These people did not hesitate to listen my progressive work report and gave me the suggestion during the group meeting.

Dr.Teeraparb Chantavat is one of the most influent person of my work. He was one of my thesis proposal's committee. His exhortation made me understand physical cosmology better.

Finally, I would like to thank my family who always stand by my side whatever I have faced. They are my motivations, my heart, my souls and my life. Without their supports, I cannot archive this work.

Anut Sangka

CONTENTS

Page

CHAPTER

CONTENTS (Continued)

CONTENTS (Continued)

LIST OF TABLES

LIST OF FIGURES

LIST OF FIGURES (Continued)

LIST OF FIGURES (Continued)

CHAPTER I

INTRODUCTION

1.1 Cosmic Microwave Background Cold Spot Anomaly

The cosmic microwave background (CMB) radiation is the earliest electromagnetic signal of the Universe that we can observe. In the hot Big Bang cosmology, CMB is the light that freely traversed after the epoch of recombination. The CMB has a black-body spectrum with a current average temperature of 2.725 K. Theoretically, the primordial CMB map is almost smooth everywhere across the Universe with very small Guassian fluctuations. The root mean square of the fluctuations is about 18 μK. Figure 1.1 is the full sky CMB temperature fluctuations map as observed by Planck satellite mission (Planck Collaboration, 2014). The red colour corresponds to slightly hotter regions than average, while the blue shows slightly colder regions. Planck's CMB map agree mostly with theoretical prediction except some strange imprint parts in CMB map such as the anomaly cold spot.

When the high precision of mathematical analysis is applied to the CMB observational data, the strange structures had been observed in CMB map. One of the strangest structures is the cold spot anomaly which first detected by NASA WMAP mission (Cruz et al., 2005). This large cold spot is located in the Southern Galactic Cap, $l \approx 209°$, $b \approx -57°$ (see Figure 1.2) with the angular radius on the sky of about $r \simeq 10°$. The temperature of the cold spot's centre is also significantly colder, $\Delta T \approx 150\mu$K, than average CMB temperature, 2.725 K ± 18 μK. In terms of size, previous works have indicated (see later) that this cold spot may be caused

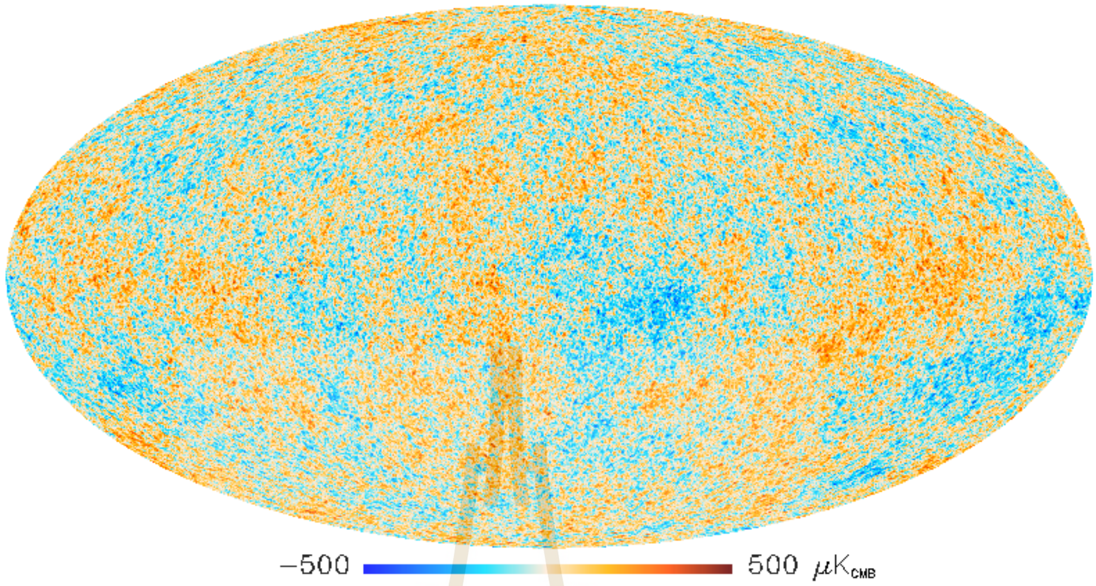

Figure 1.1 CMB temperature fluctuations map from Planck satellite mission.

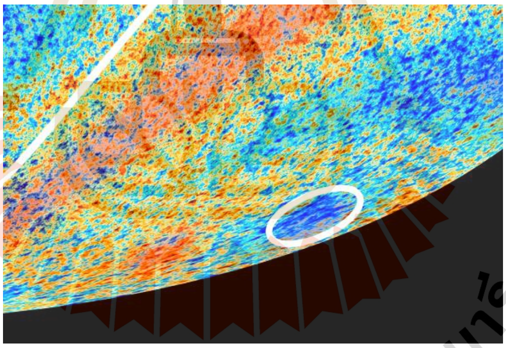

Figure 1.2 A zoom-in map of the CMB cold-spot anomaly region.

by a foreground large-scale structure located at around 600 Mpc away from us which has an inferred radius of about 200 Mpc, a third of the distance from us to the centre of cold spot. Because of the Guassian distribution and small amplitude, 1 part in 10^5, of the CMB fluctuations,, the probability that such a large structure could exist is very low (less than 0.0001). Thus, the origin of the large cold spot needed to be studied.

Recently, many studies (Szapudi et al., 2014b; Finelli et al., 2014; Szapudi et al., 2014a) proposed that the origin of the cold spot could be a super-void. The metric tensor that well describe the geometry of super-void is Lema$\hat{\imath}$tre-Tolman-Bondi (LTB) metric (Alonso et al., 2010). On large scale, the cosmic void can induce secondary CMB temperature fluctuations by Integrated Sachs Wolfe (ISW) effects. For small scale, the secondary fluctuations may be caused by non-linear ISW or weak gravitational lensing (weak lensing for short hand). The works of Szapudi et al. (2014b); Finelli et al. (2014) and Szapudi et al. (2014a) only concerned the secondary CMB temperature fluctuations from ISW effect caused by a single void and the weak lensing was not considered. Hence, it is good opportunity for us to study the large cold spot via ISW and weak lensing effect.

The rest of this chapter aims to review required background knowledge for studying CMB cold spot anomaly. The notations and conventions which will appear later in the thesis also will be establish in this chapter.

1.2 Cosmological Theory

1.2.1 The Cosmological Principle

Most of modern theoretical physics base on the symmetry which leads to the law of conservation. Unsurprisingly, the physical system that is well described by the laws of physics, also has physically symmetrical properties. In principle, the Universe is not an exception, on the large scale the Universe is the same in all direction. In addition, it is the same everywhere, and laws of physics do not depend on the location of an observer. In other words the Universe is homogeneous and isotropic on sufficiently large scales. This principle is called the cosmological principle. One of the supported evidence is the galaxy distribution, which has been shown to obey the cosmological principle on the scales larger than $100\ h^{-1}$ Mpc (Wu et al., 1999).

To study the Universe, the cosmological principle is needed to combine with theoretical physics. On cosmological scale gravity is the dominant interaction. The best modern macroscopic gravitation theory is Einstein's general relativity (GR), the theory of spacetime. GR states that spacetime is dynamic. Applying the cosmological principle to GR, it implies that the Universe must be non-static, either expanding or contracting. One of the supported evidences of this hypothesis is the observation of galaxies move away in all directions by Edwin Hubble (Hubble, 1929). This leads to the idea that the Universe is now expanding. Moreover, Type Ia supernovae observational data had shown that the Universe expands with an acceleration (Riess et al., 1998). Tracing back to history, clearly in the old time the Universe would have been much smaller than today. There should be the original state of the universe, the state that the spacetime was a singularity, where all the low of physics that we know break down, very hot and dense, the "Big Bang".

The Big Bang theory was initially proposed by Lameitre . The Big-Bang theory predict that the elementary particles was created during the first few minutes after the Big Bang. In complementary to The Big Bang, inflation caused the Universe from a single point to physical scale and give the quantum fluctuations which are the seeds of cosmic structures, e.g. galaxies, clusters of galaxy etc (Guth, 1981). These quantum fluctuations caused the tiny anisotropy on CMB which can be observed by CMB experiments such as WMAP and Planck missions.

1.2.2 The Geometry of The Universe

When the cosmological principle is applied to GR, it leads to a maximally symmetric spacetime known as FLRW (stands for Friedmann La$\hat{\imath}$metre Robertson

Walker) (Weinberg, 1972) metric tensor. This metric line element is given by

$$ds^2 = g_{\mu\nu}dx^\mu dx^\nu = -dt^2 + a(t)^2\left[\frac{dr^2}{1-\kappa r^2} + r^2(d\theta^2 + \sin^2\theta d\phi^2)\right], \tag{1.1}$$

where we sum over dummy indices μ and ν from 0 to 3. We also adopt the speed of light c to 1, t is the proper time, $a(t)$ is scale factor, r, θ and ϕ are comoving spherical coordinates. The curvature κ is a constant related to the spatial geometry of the Universe and can be 1, -1,0 correspond to open, closed and flat geometries, respectively.

The rate of expansion of the Universe $H(t)$ can be given by

$$H \equiv \frac{\dot{a}}{a}, \tag{1.2}$$

where a dot represents a conformal time t derivative. This parameter is called the Hubble parameter. Defining H_0 as the Hubble parameter at the present epoch (call Hubble constant). Recent measurements lead us to believe that the Hubble constant is very close to 70 ± 10 km s^{-1} Mpc^{-1} (Planck Collaboration, 2014). Because it still remains unclear the precise value,we often set the Hubble constant as

$$H_0 = 100h \text{ km s}^{-1} \text{ Mpc}^{-1}, \tag{1.3}$$

so that $h \approx 0.7$.

1.2.3 Dynamics of The Expanding Universe

The cosmological dynamics can be obtained by solving the Einstein equation

$$R_{\mu\nu} - \frac{1}{2}g_{\mu\nu}R = 8\pi G T_{\mu\nu}, \tag{1.4}$$

where $T_{\mu\nu}$ is the energy-momentum tensor of the matter components and G is a universal gravitation constant. The Ricci tensor $R_{\mu\nu}$ is defined by

$$R_{\mu\nu} = \partial_\alpha \Gamma^\alpha_{\mu\nu} - \partial_\nu \Gamma^\alpha_{\mu\alpha} + \Gamma^\alpha_{\mu\nu}\Gamma^\beta_{\alpha\beta} - \Gamma^\alpha_{\mu\beta}\Gamma^\beta_{\alpha\nu}, \tag{1.5}$$

where ∂_α stands for partial derivative operator

$$\partial_\alpha \equiv \frac{\partial}{\partial x^\alpha}. \tag{1.6}$$

$\Gamma^\mu_{\nu\kappa}$ is the Christoffel symbol, which can be calculated from

$$\Gamma^\mu_{\nu\kappa} = \frac{1}{2} g^{\mu\lambda}\Big[\partial_\kappa g_{\lambda\nu} + \partial_\nu g_{\lambda\kappa} - \partial_\lambda g_{\nu\kappa}\Big]. \tag{1.7}$$

Since $g_{\mu\nu}$ is symmetry in exchanging indices, consequently the Christofel symbol is also deserved the symmetry in exchanging indices. R is the Ricci scalar curvature, given by contraction of the Ricci tensor

$$R = g^{\mu\nu} R_{\mu\nu} = R^\mu_{\ \mu}. \tag{1.8}$$

With FLRW metric the non-vanish Ricci tensor components are

$$\begin{aligned}
R_{00} &= -3\frac{\ddot{a}}{a} \\
R_{11} &= \frac{a\ddot{a} + 2\dot{a}^2 + 2\kappa}{1 - \kappa r^2} \\
R_{22} &= r^2(a\ddot{a} + 2\dot{a}^2 + 2\kappa) \\
R_{33} &= r^2(a\ddot{a} + 2\dot{a}^2 + 2\kappa)\sin^2\theta.
\end{aligned} \tag{1.9}$$

and the Ricci scalar is then

$$R = 6(2H^2 + \dot{H} + \kappa/a^2). \tag{1.10}$$

We choose the matter and energy to be a perfect fluid which are at rest in comoving coordinates. The four-velocity is then

$$U^{\mu} = (-1, 0, 0, 0) \tag{1.11}$$

and the energy-momentum tensor

$$T_{\mu\nu} = (\rho + p)U_{\mu}U_{\nu} + pg_{\mu\nu}, \tag{1.12}$$

where p and ρ denote pressure and density, respectively. Furthermore, we assume that p and ρ have equation of state,

$$p = w\rho. \tag{1.13}$$

Plug in, energy momentum tensor, Ricci tensor, Ricci scalar and $g_{\mu\nu}$ metric to Einstein's equation, yield,

$$\left(\frac{\dot{a}}{a}\right)^2 = \frac{8\pi G}{3}\rho - \frac{\kappa}{a^2}, \tag{1.14a}$$

$$\frac{\ddot{a}}{a} = -\frac{4\pi G}{3}(\rho + 3p). \tag{1.14b}$$

Eq. 1.14 are known as the **Friedmann equations** the most important equation of cosmology. Multiplying Eq. 1.14a by a^2, differentiating and using Eq. 1.14b, we find

$$\dot{\rho} + 3H(\rho - p) = 0. \tag{1.15}$$

Using equation of state, this turn to be

$$\frac{\dot{\rho}}{\rho} = -3(1 + w)\frac{\dot{a}}{a}. \tag{1.16}$$

Solving this equation, we get

$$\rho \propto a^{-3(1+w)} \tag{1.17}$$

The radiations and relativistic particle such as neutrino have $w = 1/3$. The dark matter and cold gas dominate the matter sector and are considered collisionless and pressure-less, i.e. $w = 0$. In the case of vacuum energy (or Cosmological Constant Λ) that has the constant energy density and negative pressure for driving the Universe accelerated expansion, $w = -1$. The energy density evolution of Universe made up of perfect fluid dominated by these three components can be written as,

$$\rho = \rho_{\gamma,0} a^{-4} + \rho_{m,0} a^{-3} + \rho_{\Lambda}, \tag{1.18}$$

where $\rho_{m,0}$ and $\rho_{\gamma,0}$ are matter and radiation density at present epoch and $\rho_{\Lambda} \equiv \Lambda/8\pi G$. It is good to introduce another useful quantity the density parameter,

$$\Omega = \frac{8\pi G}{3H^2}\rho = \frac{\rho}{\rho_{\text{cri}}}, \tag{1.19}$$

where the critical density is defined by

$$\rho_{\text{cri}} = \frac{3H^2}{8\pi G}. \tag{1.20}$$

Eq. 1.14a now can be re-written as

$$\Omega_{\kappa} = \Omega_{\text{total}} - 1 = \frac{\kappa}{H^2 a^2}. \tag{1.21}$$

This can describe the geometry of the Universe as

$$\begin{array}{lcccccl} \rho_{\text{total}} < \rho_{\text{cri}} & \leftrightarrow & \Omega < 1 & \kappa < 0 & \leftrightarrow & \text{open} \\ \rho_{\text{total}} = \rho_{\text{cri}} & \leftrightarrow & \Omega = 1 & \kappa = 0 & \leftrightarrow & \text{flat} \\ \rho_{\text{total}} > \rho_{\text{cri}} & \leftrightarrow & \Omega > 1 & \kappa > 0 & \leftrightarrow & \text{closed.} \end{array}$$

We can use Eq. 1.18 and Eq. 1.21 to study the evolution of the scale factor $a(t)$. Figure 1.3 is the plot between $a(t)$ and time by the given density parameters (subscripted m and Λ represent matter and cosmological constant, respectively).

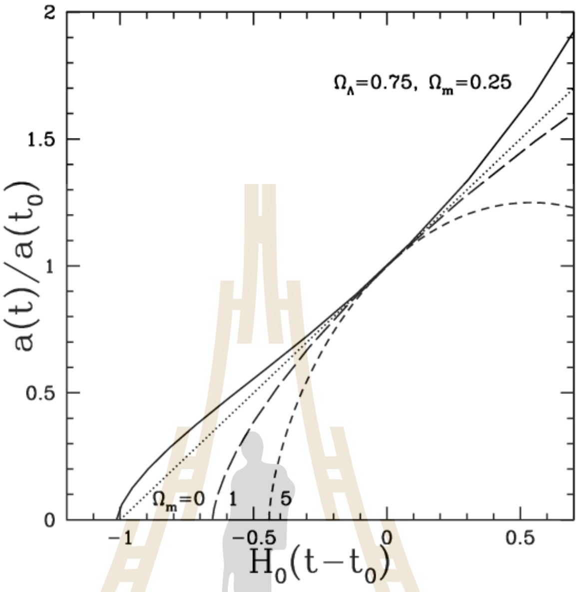

Figure 1.3 The scale factor evolutions for different density parameters.

Consider the case with $\Omega_{\mathrm{m}} = 0.25$ and $\Omega_{\Lambda} = 0.75$ which is close to the present observational data. At very beginning of spacetime ($a \ll 1$), the radiation was the dominant part of the Universe by the evolution a^{-4}. As Universe expands and a larger the matter became the main component. Eventually because the vacuum energy never dilutes in time, most part of the Universe is the vacuum energy which causes the accelerated expanding of the Universe.

1.2.4 Standard Cosmological Model: ΛCDM

The standard cosmological model base on the cosmological principle and the hot Big Bang with inflation model. The observations had been shown that Ω_{κ} is nearly to zero, in other words the Universe is spatially flat. From the density evolution, we can see that there are three main species of matter-energy in the Universe, matter, radiation and vacuum (dark) energy. The matter can be classified into two types. The ordinary or baryonic matter which can be described by the standard model of elementary particles physics. The present experiments and observations indicate that this type of matter is only 4 percent in the Universe (Lahav and Liddle, 2014). The second type is the dark matter which is approximately 25 percent of the matter-energy density Universe. The dark matter can not be seen directly but it can be indirectly observed by its gravitational effect on the rotation curve of spiral galaxies (Babcock, 1939) or by identifying distortion image of background galaxies due to the gravitational lensing (Massey et al., 2010) etc. The biggest compoent of the Universe is dark energy, which is some kind of influence that drives the Universe accelerated expanding. It is first inferred in 1998, by observation of Type Ia supernovae by the Supernova Cosmology Project (Riess et al., 1998). As mention before, the main candidate of dark energy is vacuum energy (Carroll et al., 1992) which can be characterised by cosmological constant

Λ in Einstein's field equation. the main manifest properties of dark energy are smoothly spread across the Universe and negative pressure (repulsive gravity).

1.2.5 Cosmological Distances

Because most of cosmological information come from the electromagnetic waves which are redshifted due to the expansion of space. The redshift z is defined by

$$z = \frac{\lambda_o - \lambda_e}{\lambda_e}, \tag{1.22}$$

where λ_e is the emitted wavelength of the radiation by the source at it's rest frame and λ_o is the observed wavelength by an observer at a given time. Since the light travel on null-path ($ds^2 = 0$). Hence if the light is emitted by the source at comoving coordinate r_1 at time t_1, it arrives at the origin $r = 0$ at a later time t_0, give by (FLRW metric)

$$r_{10} = \int_{t_1}^{t_0} \frac{dt}{a(t)} = \int_0^{r_1} \frac{dr}{\sqrt{1-\kappa r^2}}. \tag{1.23}$$

Since the radial coordinate r_1 of comoving source is independent on time, so the interval δt_1 between departure signals is related to the interval δt_0 between arrivals of same signals by

$$\frac{\delta t_1}{a(t_1)} = \frac{\delta t_0}{a(t_0)}. \tag{1.24}$$

This leads to the relationship between scale factor $a(t)$ and redshift z

$$a = \frac{a_0}{1+z}. \tag{1.25}$$

Normally, we set the present scale factor $a_0 = a(t_0)$ to be unity. With the definitions of z, H and Ω Friedmann's equation Eq. 1.14a can be rewritten as

$$H^2(z) = H_0^2\Big[\Omega_{\gamma,0}(1+z)^4+\Omega_{m,0}(1+z)^3+\Omega_{\Lambda,0}(1+z)^{3(1+w_\Lambda)}+(1-\Omega)(1+z)^2\Big], \tag{1.26}$$

where w_Λ is left to be arbitrary for the case that the dark energy has an evolution.

We can see that to study the Universe, it mostly involve with the measurement of $H(z)$. The measurement techniques such as using supernovae Ia as standard candles or standard ruler from the Baryon Acoustic Oscillation (BAO) and the acoustic peak scales in the CMB fluctuations, all measure $H(z)$ in the form of either 'Angular Diameter Distance' (d_A) or 'Luminosity Distance' (d_L) as a function of redshift,

$$d_A(z) = \frac{d_L(z)}{(1+z)^2} = \frac{r}{1+z} = \frac{1}{(1+z)H_0\sqrt{|\Omega_\kappa|}} f_\kappa\left[H_0\sqrt{|\Omega_\kappa|}\int_0^z \frac{dz'}{H(z')}\right], \qquad (1.27)$$

where $f_\kappa(x) = \sin(x),\ x$, or $\sinh(x)$ for closed, flat, and open models, respectively.

1.3 Observational Cosmic Microwave Background Radiation

In spite of the fact that, theoretical physicists had predicted CMB since 1950s. The prediction was suspected until 1964 when it was confirmed by the accidental detection by Arno Penzias and Robert Woodrow Wilson who worked at Bell Labs in Holmdel, New Jersey. Intially, they were experimenting with a supersensitive radio antenna. Even with several methods which were used to reduced noise as much as possible, there still was the mysterious background noise coming from all direction of sky. This background noise was estimated to have antenna temperature of 3.5 ± 1.0 K at 7.3 cm wavelength which was close to the prediction by Alpher and Herman (Alpher, 1948). Later on, Penzias and Wilson shared their discovery with Dicke, Peebles, Roll and Wilkinson (Penzias and Wilson, 1965) who were making the experiment to detected CMB signal. The two groups published their results and interpreted the mysterious background noise as

CMB signal from Big Bang.

The space-base CMB experiment is called the NASA's COsmic Background Explorer (COBE) (Boggess et al., 1992) satellite mission launched in November 1989. This experiment had measured CMB spectrum between 60-600 GHz and shown that it has a blackbody spectrum (see Figure 1.4). The best evaluation of CMB temperature made with four-year COBE data is $T_o = 2.725 \pm 0.002$ K. COBE can measure the CMB fluctuation on scales larger than about 7^o. The measurement by COBE had been shown that the CMB temperature map almost uniform. Consider Figure 1.5, the more blue means the lower temperature while the more red means the hotter. Figure 1.5 illustrate that the fluctuation of CMB temperature is roughly 1 μK which only is 1 part in 10^5 of average temperature of CMB.

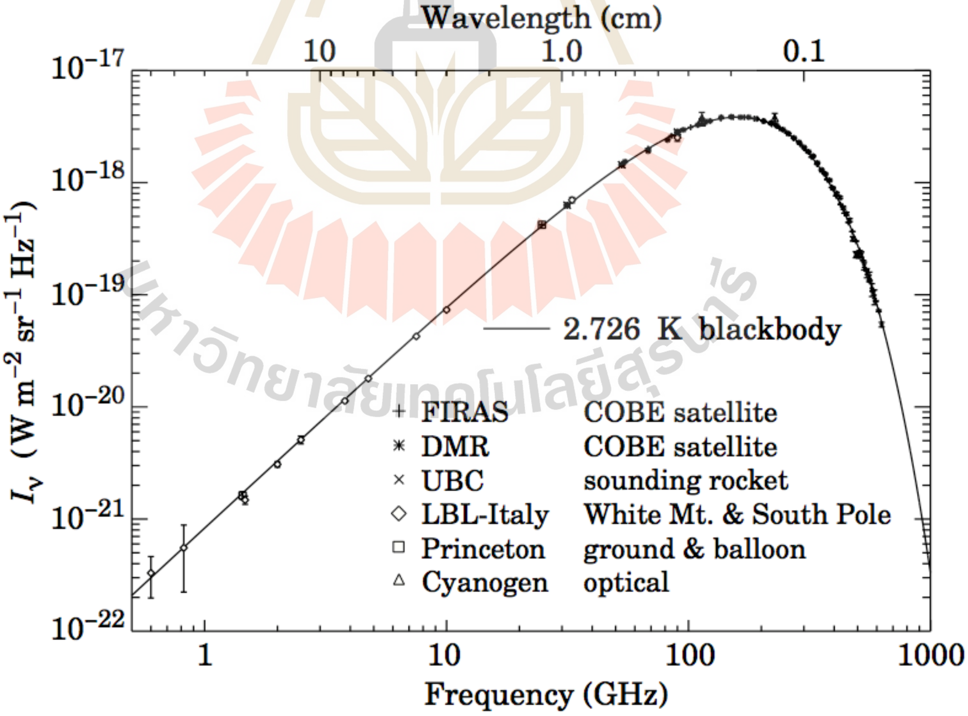

Figure 1.4 CMB measurement spectrum: The spectrum is almost identical to blackbody spectrum with the temperature $T = 2.725$ K (Banday et al., 1997).

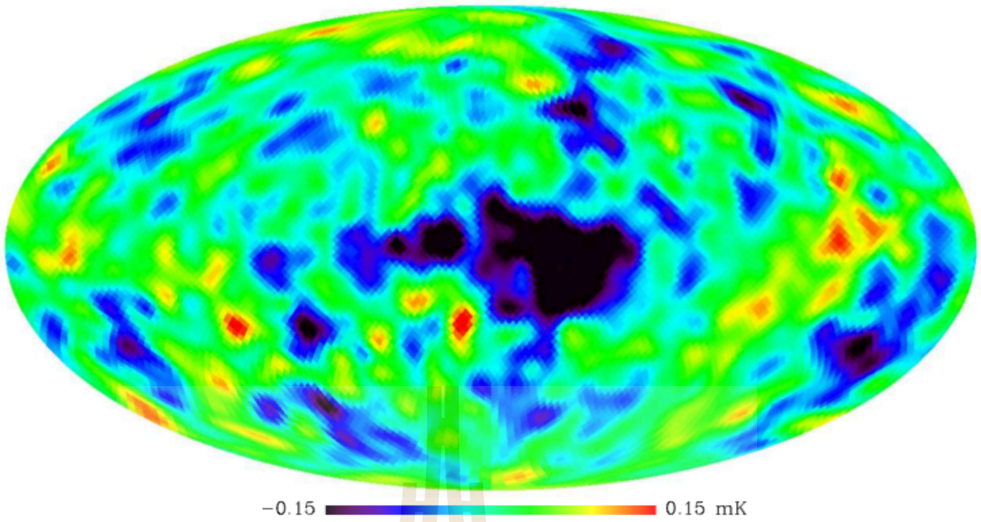

Figure 1.5 CMB temperature map by COBE.

The successor of COBE satellite mission is the more advance satellite mission which also was sent by NASA, the Wilkinson Microwave Anisotropy Probe (WMAP) satellite mission. WMAP was improved sensitivity and angular resolution 45 and 33 times to COBE respectively. The main aims of WMAP are studying the density perturbation of the early Universe and the mysterious dark energy. The WMAP's data played a key role in establishing ΛCDM. The measurements are well fitting the cosmological constant (Λ) of dark energy model. But some unexpected results are also detected including the cold spot anomaly which its original is the main topic in this thesis.

The most recent space base experiment is ESA's (European Space Agency) Planck satellite mission. Planck carries two scientific instruments. An 56 radio receivers are installed in the Low-Frequency Instrument (LFI) which well respond to 30-100 GHz emission. It operates at 20K and provides angular resulotion 10 arc of minute and 12 μK sensitivity. The second instrument is High-Frequency Instrument (HFI) bears 56 bolometres sensitive to 100-850 GHz emission. It can work at 0.1 K and provides angular resolution about 5 arc of minute and roughly

5 μK sensitivity. The Planck telescope is 1.5 m in diameter.

Planck is purposed to measure the B-mode polarisation of CMB due to the gravitational radiation from “Inflation” epoch and study the origin of cosmic structure. Planck’s measurement results still remain the results of WMAP. The cosmological parameters are only slightly different from WMAP’s measurement. The anomaly cool spot is still noticeable in Plank’s CMB temperature map. While most of Planck’s data is well satisfied with Inflationary cosmology, the significant evidence of B-mode CMB polarisation still remains undetected.

1.4 Cosmic Voids

The local regions of the Universe can be separated to two regions, over-dense regions which called cluster (of galaxies) and cosmic voids which is the under-dense region. The cosmic void is vast region with very lower density than the cosmic average. It was first discovered by Gegory and Thompson in 1978. Voids typically have a diameter of size of 11 to 150 Mpc. A very large voids is called super-void. Cosmic voids can cause secondary anisotropy of CMB due to linear Integrated Sachs Wolfe (ISW) on large scale or Ree Scima (nonlinear ISW), gravitational lensing and SZ effects on small scale. In Big-Bang cosmology framework, cosmic voids could be formed by baryon acoustic oscillations. Originally, start from small quantum fluctuations in the early Universe and evolve to density anisotropies. Higher density regions collapsed under gravity, finally form the cosmic web of voids and galaxy filaments seen today.

There are three main methods for finding voids. The first method is called VoidFinder algorithm (Hoyle and Vogeley, 2002). This method directly find the empty regions of space base on local galaxy density. Normally, this method assumes the spherical shape of void. The body, edge and wall of void are well defined in the algorithm. The density around the centre is roughly 10 % of mean cosmic density and quickly rises to 20% at the edge and then 100% in the walls outside the edge.

The second algorithm is ZOBOV (Zone Bordering on Voidness) algorithm (Sutter et al., 2012). Unlike, VoidFinder Algorithm which consider density of space directly, this method try to find void by consider the geometrical structures in the dark matter distribution. Initially the method was introduced with no parameter and presumed shape. This method can find the shape and size of void very well. However, it mostly finds small and trivial voids. The method can be improved efficiency by applying the physical parameters such as a minimum density.

The last method is called DIVA (Dynamical Void Analysis) algorithm. This method considers voids from different perspective. Voids can be redefined as a region in which matter is escaping; which corresponds to the dark energy equation of state, w. The centres of void now are the maximal source of displacement field of matter. This method was introduced for studying of evolution of voids in large scale structure. Due to the different definition of void the outcomes of this method now differ from two previous methods (Hahn et al., 2007).

Now, there are many catalogues of voids which publish online for example the work of (Sutter et al., 2012) which is the outcome from Sloan Digital Sky Survey Data Release 7 (SDSS DR7) galaxy redshift surveys. ZOBOV algorithm was used in this catalogue. Figure 1.6 shows void population map in redshift range 0.05 to 0.1. From Figure 1.6 and other plots in (Sutter et al., 2012) we can refer that typical radius of void should be $15 < r_{\mathrm{v}} < 25$ Mpc h^{-1}.

In this work we consider three void density profiles. The first one is the Hamuas, Sutter and Wandelt (HSW) void density profile, the second is LTB model and the last is multivoid model.

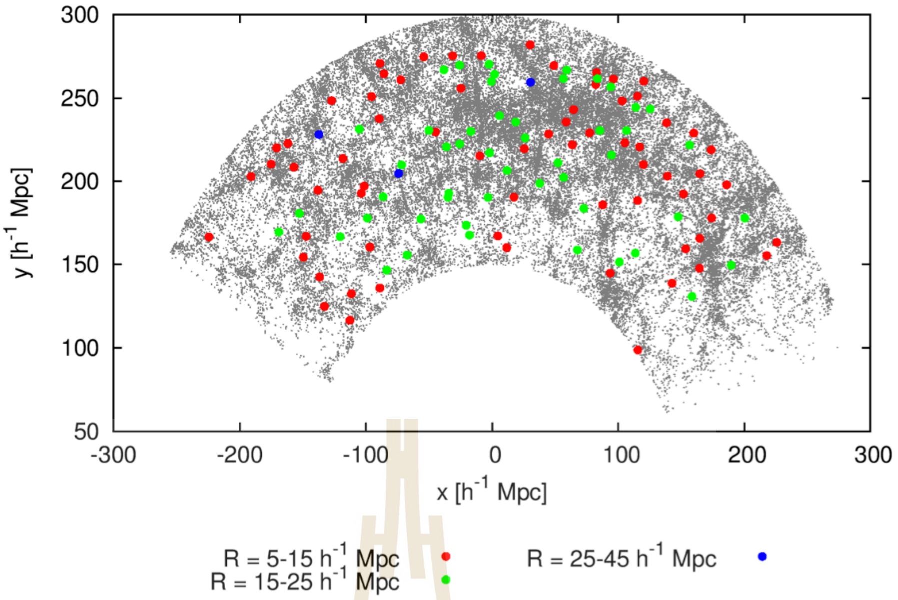

Figure 1.6 The voids distribution from redshift 0.05 to 0.1 : The galaxies are represented in grey while voids are represents in colour depending on the size as indicated in the plots.

1.4.1 HSW Void Density Profile

In 2014, HSW propose a simple empirical function for the average density profile of cosmic voids (Hamaus et al., 2014). The method of their research is the watershed technique in ΛCDM N-body simulations. Initially, they used four parameters model to simulated the density profile. Later on, the simulations had shown that two of four parameters to be redundant as they follow linear trends with the scale radius. So, this void model has only two parameters to characterised void density, scale radius $r_{\rm s}$ and central density contrast $\delta_{\rm c}$. Given $\rho_{\rm v}$ is the density of void, $\bar{\rho}$ is the mean cosmic density and the void characteristic radius is denoted by $r_{\rm v}$. The density contrast of void can be described as,

$$\frac{\rho_{\rm v}}{\bar{\rho}} - 1 = \delta_{\rm c}\frac{1-(r/r_{\rm s})^{\alpha}}{1+(r/r_{\rm v})^{\beta}}. \qquad (1.28)$$

α and β have approximately linear relation with $r_\mathrm{s}/r_\mathrm{v}$ by following,

$$\alpha(r_\mathrm{s}/r_\mathrm{v}) \simeq -2(r_\mathrm{s}/r_\mathrm{v} - 2), \tag{1.29}$$

$$\beta(r_\mathrm{s}/r_\mathrm{v}) \simeq \begin{cases} 17.5 r_\mathrm{s}/r_\mathrm{v} - 6.5 & \text{for } r_\mathrm{s}/r_\mathrm{v} < 0.91, \\ -9.8 r_\mathrm{s}/r_\mathrm{v} + 18.4 & \text{for } r_\mathrm{s}/r_\mathrm{v} \geqslant 0.91. \end{cases} \tag{1.30}$$

Since it is very useful in the future to written Eq. 1.28 as the function of $x = r/r_\mathrm{v}$,

$$\delta_\mathrm{H}(x) \equiv \frac{\rho_\mathrm{v}}{\bar{\rho}} - 1 = \delta_\mathrm{c} \frac{1 - \sigma x^\alpha}{1 + x^\beta}, \tag{1.31}$$

where $\sigma = (r_\mathrm{s}/r_\mathrm{v})^{-\alpha}$. The physical meaning of r_s is a radius at which $\rho_\mathrm{v} = \bar{\rho}$. The well fitting from profile Eq. 1.28 to observational data is illustrated by Figure 1.7. One of the special features of the HSW profile is that its include positive density contrast region (so called void compensation) (Hamaus et al., 2014) while other (normal) void density profiles do not include. Figure 1.7 had been shown that HSW profile can describe void compensation quite well.

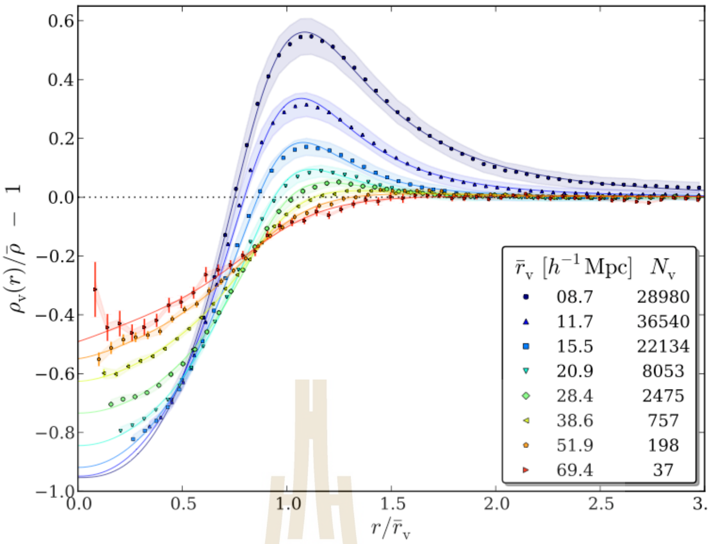

Figure 1.7 Stacked density profiles of voids at redshift zero in eight set of voids of size. The shade regions represent the standard deviation σ of each stacks (scaled down by 20 for visibility), while error bars come from standard errors on the mean profile $\sigma/\sqrt{N_{\rm v}}$. The solid lines is the best fit solution from density profile Eq. 1.28 (Hamaus et al., 2014).

Moreover, the well description of HSW profile, there is the *Universality* property in HSW profile as shown by relationship of α, β and $r_{\rm s}/r_{\rm v}$. $\delta_{\rm c}$ and $r_{\rm v}$ also have interested nonlinear relationship as shown by Figure 1.8. Because there is still some uncertainty in $\delta_{\rm c}$ and $r_{\rm v}$ then we should leave $\delta_{\rm c}$ as a free parameter.

1.4.2 LTB Model

LTB model is the short name of LTB geometry embedded in ΛCDM of cosmic void model. Basically, LTB geometry is just the more general version of FLRW geometry. The scale factor $a(t)$ now depend both on time and space $A(r,t)$,

$$ds^2 = -dt^2 + \frac{(A'(r,t)^2)}{1-\kappa(r)}dr^2 + A(r,t)^2(d\theta^2 + \sin^2\theta d\phi^2), \tag{1.32}$$

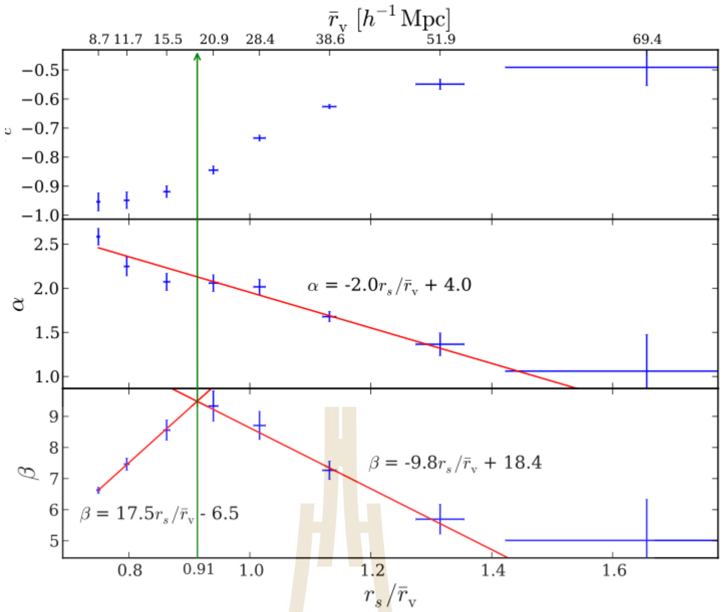

Figure 1.8 Shows relationship between parameters, α and β clearly have linear relationship with r_s/r_v. While relationship between δ_c and r_v seems to be nonlinear. The picture is taken from Hamaus et al. (2014)

where $\kappa(r)$ is the curvature function which now depends on coordinate and $A'(r,t) = \partial A(r,t)/\partial r$. In order to make this geometry embedded to ΛCDM we need $\kappa = 0$ at r becomes larger and larger. From the works of Finelli et al. (2014), we can suppose that,

$$\kappa(r) = \kappa_0 r^2 \exp(-r^2/r_v^2). \tag{1.33}$$

This curvature leads to Newtonian potential Φ_L,

$$\Phi_L(\tilde{r}) = \Phi_0 \exp(-\tilde{r}^2/\tilde{r}_v^2). \tag{1.34}$$

with an LTB radius r defined as $\tilde{r} = \sqrt{3/4\pi} H_0 r$ using the co-moving FLRW radius r. The corresponding to the 3D density profile of Φ_L is,

$$\delta_L(\tilde{r}) = \delta_c \left(1 - \frac{2\tilde{r}^2}{3\tilde{r}_v^2}\right) e^{-\frac{\tilde{r}^2}{\tilde{r}_v^2}}. \tag{1.35}$$

The benefit of this model is if dose not require N-body simulation to get density profile like HSW profile. The only thing that we need to do is finding the appropriated $\kappa(r)$. The comparison between WISE-2MASS and 2D projection of δ_L (denoted as δ_2D) by Finelli et al. (2014), displays in Figure 1.9.

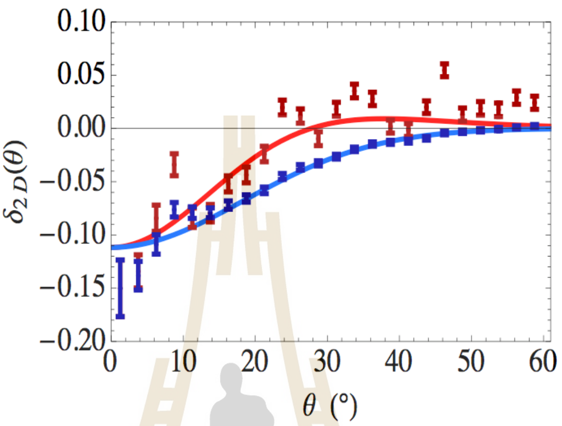

Figure 1.9 The 2D density profile from WISE-2MASS catalogue compared with the theoretical model. The plot is produced by Finelli et al. (2014)

1.5 ISW Effect

The ISW effect is caused by the change in energy of CMB photons as they traverse the linear changing of gravitational potentials (Cai et al., 2009) (Cai et al., 2010). If gravitational potential nonlinearly evolves then the ISW effect becomes nonlinear effect which has alternative name as the Ree-Sciama (RS) effect. When CMB photons travel through an over dense region, such as galaxy cluster, will gain more energy falling into the potential well than it later loses climbing out of the evolved shallower potential well. Consequently, overdense regions correspond to hot regions in a linear ISW map. In contrast, as voids are underdense regions they appear cold in linear ISW map. If the geometry of the universe is spatially flat as described by FLRW metric tensor then the ISW effect only occurs if and only if dark energy exist. So, the ISW effect is a suitable tool to study dark energy dynamics.

Let $\Delta T_{\mathrm{ISW}}(\hat{n})$ be the induced temperature caused by ISW effect in $\hat{n}$ direction on the sky and $\bar{T}$ is the mean temperature. The ratio between these qualities can be calculated by

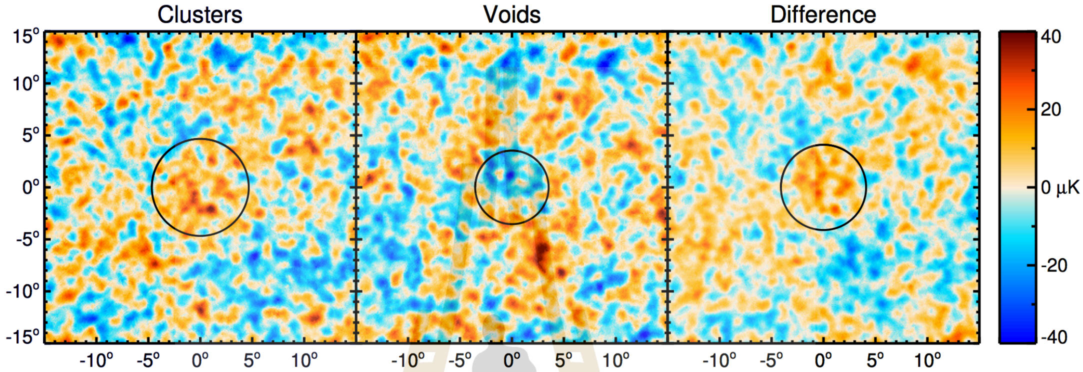

Figure 1.10 Appearance of ISW effect on CMB map which is observed by Planck. Left panel shows the result from stacking of 50 supercluster, the middle is the results from stacking of 50 voids and right panel shows the difference between both result. It is clearly that the ISW effects due to the cluster appear hot in CMB map while voids give the cold region. The picture is taken from Planck Collaboration et al. (2014).

$$\frac{\Delta T_{\mathrm{ISW}}}{\bar{T}}(\hat{n}) = -2\int_{0}^{\tau_L} \dot{\Phi}(\tau,\hat{n})d\tau, \tag{1.36}$$

where $\dot{\Phi}$ is the time derivative of the gravitational potential, τ is the conformal loopback times, with $\tau = 0$ at the present and $\tau = \tau_L$ at the last scattering surface. The gravitational potential Φ relates to Hubble parameter H_0, matter density parameter Ω_{m} and the density contrast δ, by the Poisson equation,

$$\nabla_{\chi}^{2}\Phi = \frac{3H_0^2}{2}\Omega_{\mathrm{m}}\frac{\delta}{a}, \tag{1.37}$$

where the subscript χ denotes the derivative with respect to coormoving coordinates and $\nabla_\chi = a\nabla$, where ∇ is derivative with respect to physical coordinates (recall $\chi = ar$)

Once we find the solution of Eq. 1.37, we can evaluate the ISW effect by using Eq. 1.36. Figure 1.11 illustrates the ISW effect detected by Sawangwit and his team (Sawangwit et al., 2010) by cross-correlating galaxy samples as the tracer of large-scale structure with the WMAP CMB maps. From left to right, the galaxy samples at different redshifts. From bottom to top, showing the study using different frequency in the microwave bands. From Figure 1.11, it is very clear that the ISW effect remains the same in the various of frequency bands. It implies that ISW effect is independent of frequency which confirms that the ISW effect as an achromatic effect.

1.6 Weak Gravitational Lensing Effect

It is recommended for readers who want to comprehend in deep down level of weak lensing to read the article of Bartelmann and Schneider (Bartelmann and Schneider, 2001). In this review, we will only cover applications of weak gravitational lensing on CMB fluctuation.

Gravitational lensing effect is the effect that the light path is deflected by gravitating bodies due to the curve spacetime. It was predicted by Einstein's general theory of relativity. In cosmological scale the most important type of gravitational lensing is weak lensing (Bartelmann and Schneider, 2001). While ISW effect directly changes temperature of photon, the weak lensing does not change temperature of photon but it changes photon's trajectory which means changing in CMB temperature map. By studying distortion of image caused by gravitational lensing we can study the mass distribution in universe.

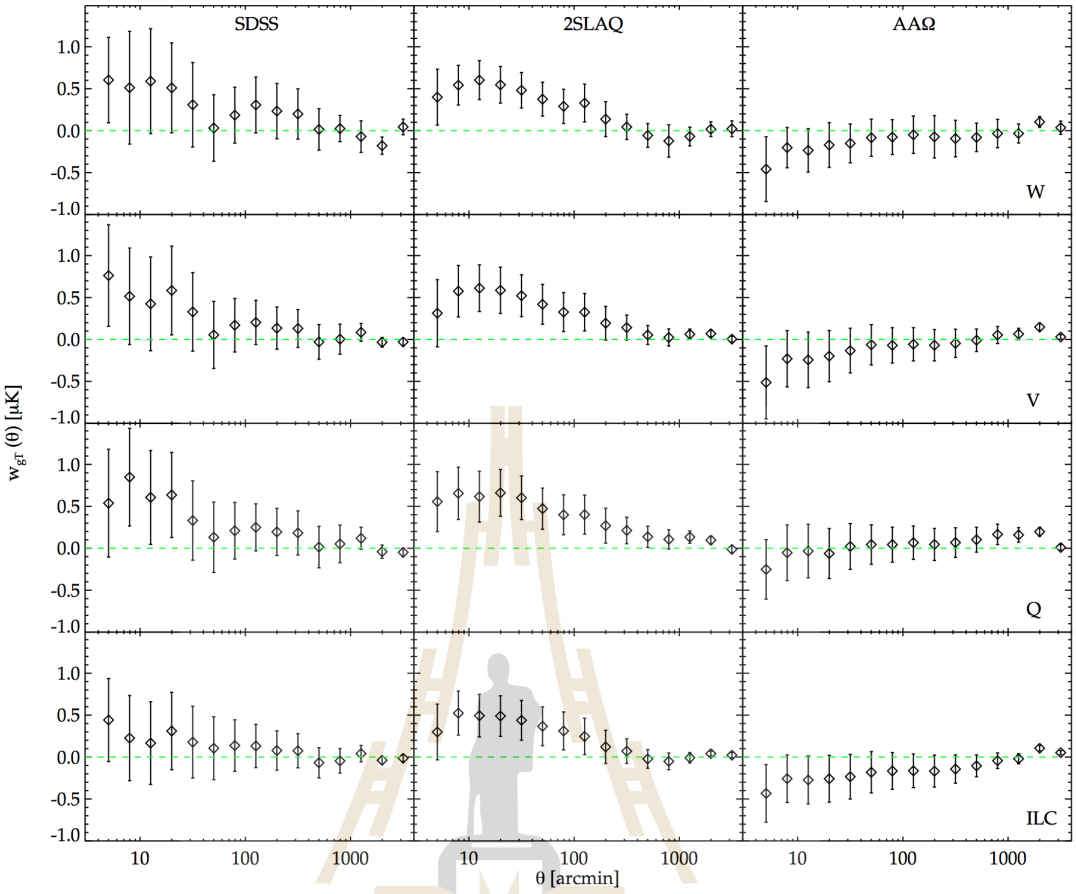

Figure 1.11 The ISW effects, observed by Sawangwit and his colleagues. This picture is captured from Sawangwit et al. (2010).

Suppose, there is a point mass M in free space. According to general relativity theory, this mass could cause curved spacetime. Since the light's trajectory is the null geodesic on spacetime. So the light ray is deflected by an angle $\hat{\alpha}$, which called deflection angle, as illustrated by Figure 1.12.

If the gravitational field is weak then general relativity predicts that deflection angle is,

$$\hat{\alpha} = \frac{4GM}{\xi}. \tag{1.38}$$

Where, ξ is impact parameter and G is Newton's universal gravitational constant.

Now consider a three-dimensional mass distribution with volume density

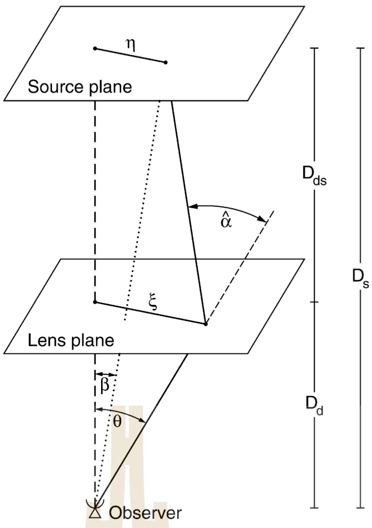

Figure 1.12 Sketch of a typical gravitational lens system which is drew by Bartelmann and Schneider (2001).

$\rho(\vec{r})$. The mass $\mathrm{d}m$ correspondence to volume $\mathrm{d}V$ is $\mathrm{d}m = \rho(\vec{r})\mathrm{d}V$. Spatial trajectory of light ray that pass this mass distribution is described by $(\xi_1(\lambda),\xi_2(\lambda),r_3(\lambda))$, where the coordinates are chosen such that the incoming light ray propagates along r_3. If the deflection angle is small, the light ray can be approximated as straight line in the neighbourhood of deflecting mass. Then, $\vec{\xi}(\lambda) \equiv \vec{\xi}$, independent of the affine parameter λ. Recognise that $\vec{\xi} = (\xi_1, \xi_2)$ is a two dimensional vector. The impact vector of the light ray relative to the mass element dm at $\vec{r} = (\xi_1', \xi_2', \xi_3')$ is then $\vec{\xi} - \vec{\xi}'$, independent of r_3', and the total deflection angle is

$$\hat{\vec{\alpha}} = \frac{4G}{\sum} dm(\xi_1', \xi_2', \xi_3') \frac{\vec{\xi} - \vec{\xi}'}{|\vec{\xi} - \vec{\xi}'|^2} \tag{1.39}$$

$$= 4G \int d^2\xi' \int dr_3' \rho(\xi_1', \xi_2', r_3') \frac{\vec{\xi} - \vec{\xi}'}{|\vec{\xi} - \vec{\xi}'|^2}, \tag{1.40}$$

which is also a two-dimensional vector. The first integral along the line of sight can be defined as the *surface mass density*

$$\Sigma(\vec{\xi}) = \int dr_3 \rho(\xi_1, \xi_2, r_3), \tag{1.41}$$

which is interpreted as the mass density projected onto a plane perpendicular to the incoming light ray. Hence, the deflection angle can be evaluated by

$$\hat{\vec{\alpha}}(\vec{\xi}) = 4G \int d^2\xi' \Sigma(\hat{\xi}') \frac{\vec{\xi} - \vec{\xi}'}{|\vec{\xi} - \vec{\xi}'|^2}. \tag{1.42}$$

This expression is valid as long as the deflected path is small which is good for weak lensing regions. Now, consider Figure 1.12, from geometrical point of view, the actual position of the object on source plane $\vec{\eta}$ is

$$\vec{\eta} = \frac{D_{\rm s}}{D_{\rm d}} \vec{\xi} - D_{\rm ds} \hat{\vec{\alpha}}, \tag{1.43}$$

where $D_{\rm s}$, $D_{\rm d}$ and $D_{\rm ds}$ are angular diameter distances. Introducing angular coodinates by $\vec{\eta} = D_{\rm s}\vec{\beta}$ and $\vec{\xi} = D_{\rm d}\vec{\theta}$, we can transform Eq. 1.43 to

$$\vec{\beta} = \vec{\theta} - \frac{D_{\rm ds}}{D_{\rm s}} \hat{\vec{\alpha}}(D_{\rm d}\vec{\theta}) \equiv \vec{\theta} - \vec{\alpha}(\vec{\theta}), \tag{1.44}$$

where we defined the scaled deflection angle $\vec{\alpha}(\vec{\theta})$ in the last step. Eq. 1.44 can be interpreted as a source with true position $\vec{\beta}$ can be seen by an observer at angular position $\vec{\theta}$ satisfying Eq. 1.44. If Eq. 1.44 has more than one solution for fixed $\vec{\beta}$, a source at position $\vec{\beta}$ has several images on the sky, i.e. the lens produces multiple images. The type of lens is *strong*. This can be quantified by the dimension-less surface mass density

$$\kappa(\vec{\theta}) = \frac{\Sigma(D_{\rm d}\vec{\theta})}{\Sigma_{cri}} \quad \text{with} \quad \Sigma_{cri} = \frac{1}{4\pi G} \frac{D_{\rm s}}{D_{\rm d} D_{\rm ds}}, \tag{1.45}$$

where Σ_{cri} is called the critical surface mass density. A mass distribution which has $\kappa \geq 1$ somewhere, i.e. $\Sigma \geq \Sigma_{cri}$, produces multiple images for some source positions $\vec{\beta}$ (see (Bartelmann and Schneider, 2001)). Consequently, Σ_{cri} is a characteristic value for the surface mass density which distinguishes between *weak* and *strong* lenses. Note that $\kappa \geq 1$ is sufficient but not necessary for producing multiple images. In terms of κ, the scaled deflection angle is

$$\vec{\alpha}(\vec{\theta}) = \frac{1}{\pi}\int_{\mathbb{R}} d^2\theta' \kappa(\vec{\theta'}) \frac{\vec{\xi} - \vec{\xi'}}{|\vec{\xi} - \vec{\xi'}|^2}. \tag{1.46}$$

Eq. 1.46 implies that deflection angle can be written as the gradient of the *lensing potential*,

$$\psi(\vec{\theta}) = \frac{1}{\pi}\int_{\mathbb{R}^2} d^2\theta' \kappa(\vec{\theta'}) \ln|\vec{\theta} - \vec{\theta'}|, \tag{1.47}$$

as $\vec{\alpha} = \nabla_\theta \psi$. The potential $\psi(\vec{\theta})$ is two-dimensional analogue of the Newtonian gravitational potential and satisfies two-dimensional Poisson equation $\nabla^2_\theta \psi(\vec{\theta}) = 2\kappa(\vec{\theta})$. In addition to Eq. 1.47 , if we known the Newtonian potential Φ we can calculate ψ by

$$\psi(\vec{\theta}) = 2\frac{D_{\mathrm{s}}}{D_{\mathrm{d}} D_{\mathrm{ds}}} \int \Phi(\vec{\theta}, \chi) d\chi, \tag{1.48}$$

where the integration has performed along the line of slight (χ).

Since weak lensing deflect the light ray, so when we observe CMB temperature the temperature map could be changed from the origin. The lensed CMB temperate anisotropy in the direction $\hat{n}$ on the sky, $\tilde{T}(\hat{n})$ equivalent to an unlensed anisotropy $T(\hat{n} + \hat{\alpha})$. Because the deflection angle $\hat{\alpha}$ is very small, consequently we can use Taylor's expansion to approximate $\tilde{T}(\hat{n})$ as below

$$\tilde{T}(\hat{n}) = T(\hat{n}) + \alpha_i \partial^i T(\hat{n}) + \frac{1}{2}\alpha_i \alpha_j \partial^i \partial^j T(\hat{n}) + O(\alpha^3). \tag{1.49}$$

1.7 This Thesis

In this study we will consider both void profile motivated by N-body simulations in standard cosmological model (ΛCDM:Lambda Cold Dark Matter) and LTB theoretical void model embedded in the ΛCDM universe. Moreover, the very large and improbable size of the super-void required to explain the anomaly is also of our interest. This work will also investigate whether the anomaly temperature profile can be described by multiply aligned voids with typical size rather than a single super-void which is at odd with our current understanding of structure formation theory of the universe.

CHAPTER II

CMB COLD SPOT MEASUREMENT

2.1 Planck Data

In previous chapter the CMB observations had been introduced. As mention before the most recent CMB observation is the Planck satellite mission. The Planck's frequency bands are separated into nine bands between 30 and 857 GHz (Planck Collaboration, 2014). The detector of the Low Frequency Instrument (HFI) are pseudo-correlation radiometers, covering bands centred at 30, 44, and 70 GHz. Complementary, the High Frequency Instrument (HFI) detectors are bolometers, covering bands centred ad 100, 143, 217, 353, 545 and 857 GHz. According to Planck Collaboration (2014) Planck delivers foreground cleaned CMB maps by using four different methods: NILC, COMMANDER, SEVEM and SMICA. The detail of these products is described in Planck Collaboration (2014); Planck Collaboration et al. (2015), the following subsection is only the summary.

2.1.1 Data Product Descriptions

1. NILC

   The Needled-ILC CMB map is included the total intensity from all frequency channel (Planck Collaboration et al., 2015). It is also constructed in polarisation, Q and U Stokes parameters, from frequency channels 30 to 353 GHz. It is obtained by applying the Internal Linear Combination (ILC) technique in needled space. The multipoles of this methods is maximum at $l = 4000$.

The angular resolution of this beam is Gussian circular beam with the 5 arcminutes of beam width.

2. COMMANDER

   Base on Bayesian parametric component separation, COMMANDER is a Planck software code which is modelled by a small number of free parameters per pixel, for example an amplitude at a given reference frequency. The COMMENDER sky maps have different angular resolutions depending on data products.

3. SEVEM

   SEVEM's CMB maps are constructed by using a procedure based on template fitting in real space in several frequencies. Normally, the templates are produced from the lowest and highest Planck frequencies and the subtracted from the CMB-dominated channels. There are no assumptions about the foregrounds or noise during the cleaning CMB map process. The intensity of CMB maps have the 5 arcminutes standard resolution with the maximum $l = 4000$. For polarisation of CMB maps have Gaussian beam width at 10 arcminutes and maximum $l = 3071$.

4. SMICA

   The linear combination of all Planck input channels with multipole-dependent weight is used to produced SMICA CMB maps. The maximum multipole of SMICA is $l = 4000$. While NILC produces both total intensity and polarisation in the single map, on the other hand the intensity and polarisation maps are produced separately. Like SEVEM SMICA intensity CMB maps have the 5 arcminutes resolution. For the polarisation maps the resolution is 10 arcminutes. The foreground signals such as the radiation in galactic plane are excluded to clean CMB signal.

2.1.2 Our Data

The temperature map that we use in this study, is Planck SMICA 2015 because it includes all frequency channels data and cleans galactic plane foreground signals. The temperature map is provided in "Fits" file format and can read by HEALPix software libraries package. HEALPix is an acronym for Hierarchical Equal Area isoLatitude Pixelation of a sphere. As suggested in the name, this pixelation produces a subdivision of a spherical surface in which each pixel covers the same surface area as every other pixel. Originally, HEALPix is aimed to use particular for CMB experiments (Gorski et al., 1999). But now it even is used in geography. The HEALPix software is available in C, C++, Fortran90, IDL, Java and Python. In this thesis we use C - HEALPix (called Chealpix) and Python - HEALPix (called Healpy). The picture of cold spot is shown by Figure 2.1.

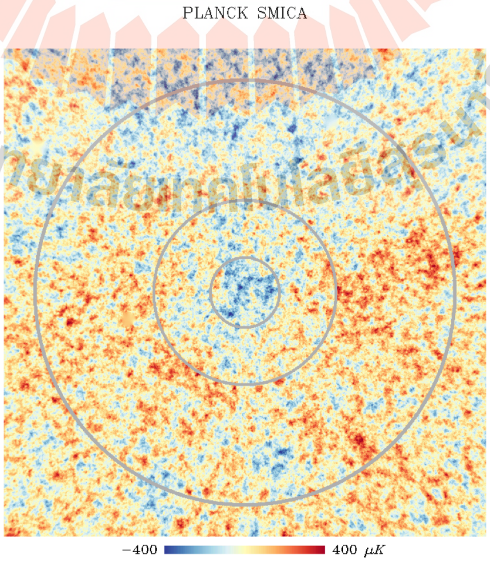

Figure 2.1 Planck SMICA CMB fluctuation in the direction of the Cold Spot. Circles correspond to 5°, 13° and 28° radii (Finelli et al., 2014).

HEALPix map surface is a unit sphere. Labelling coordinate by (θ, ϕ) or in cartesian (x, y, z), θ sweep from north pole to south pole π radius, while ϕ starts from galactic centre and the sweep in the direction from east to west by 2π radius. This differs from Galactic - Coordinate convention by IAU. So the galactic coordinate of cold spot (l = 209°, b = -57°) corresponds to ($\theta = 0.8167\pi$, $\phi = 1.1611\pi$).

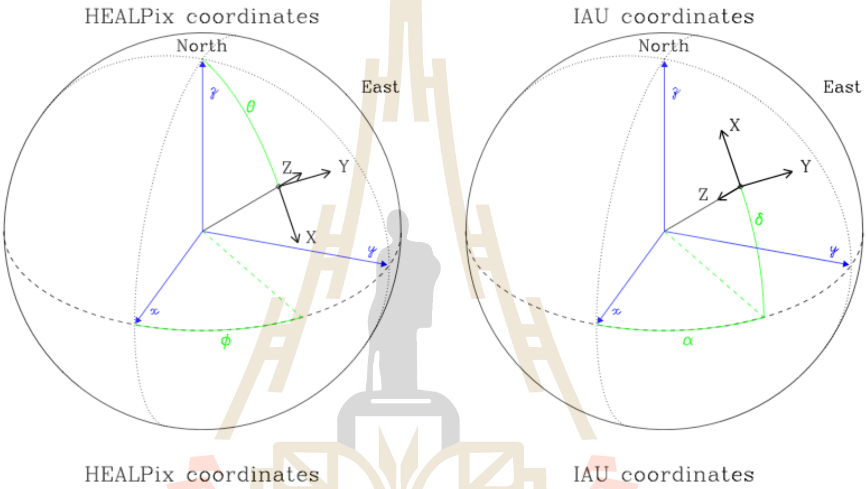

Figure 2.2 Coordinate conventions for HEALPix (left hand side panel) and IAU (right hand side panel).

2.2 1D Cold Spot Temperature Profile

We can get the 1D cold spot temperature profile by average temperature inside of cold spot's rings. In the work we divide the cold spot with the radius 30° into 30 rings. Each ring has the same thick 1°.

We can identify each points (x, y, z) inside our rings by find the dot product of (x, y, z) and the centre of cold spot (x_0, y_0, z_0). For example, if we want to know the 1D - temperature at 1.5° apart from the centre of void, we first find the

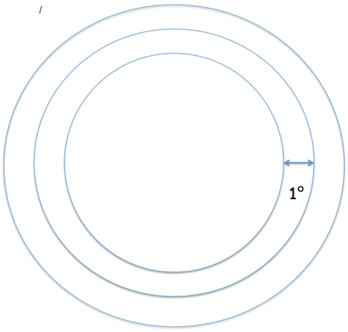

Figure 2.3 Illustrate the rings of cold spot.

points inside the disk with radius 1°. The points inside the disk are given by

$$\cos(1^{o}) < x \cdot x_0 + y \cdot y_0 + z \cdot z_0 \leqslant 1. \tag{2.1}$$

Then we can use HEALPix to find which pixels associate to these points. When we get pixel indices we will get temperature of those points. The average temperature inside angular radius θ_0 can be calculated,

$$T_0 = \frac{1}{n} \sum_{\theta<\theta_0} T(\theta), \tag{2.2}$$

where n is the total pixel inside the circle. For example, the average temperature at $\theta = 1.5$ degree is

$$T(\theta = 1.5) = \frac{1}{N_2} \sum_{\theta<2^{\circ}} T(\theta) - \frac{1}{N_1} \sum_{\theta<1^{\circ}} T(\theta), \tag{2.3}$$

where N_1 and N_2 are the number of pixel inside the rings withe angular radius 1 and 2 degree respectively. Figure 2.4 illustrates the 1D temperature profile of cold spot with the error bars which come from the normal CMB fluctuations. Figure 2.4 shows the CMB cold spot temperature profile. The error bar for each angular bin is calculated from variance of the measurements of 1000 Monte Carlo simulation. CMB maps were generated by using Syncfast function in HEALPIX software library. This Syncfast function use the angular power spectrum as a input file. In the simulations we use angular power spectrum from SMICA catalogue. The simulations had shown that the uncertainty of CMB fluctuations is scale independent as shown in Figure 2.5 which is very close to 18 μK.

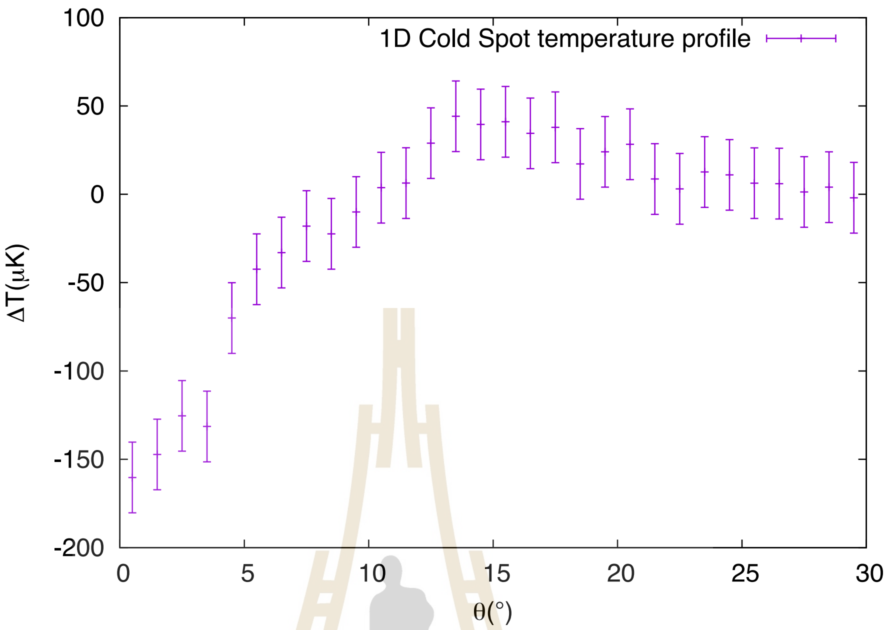

Figure 2.4 CMB cold spot 1D temperature profile

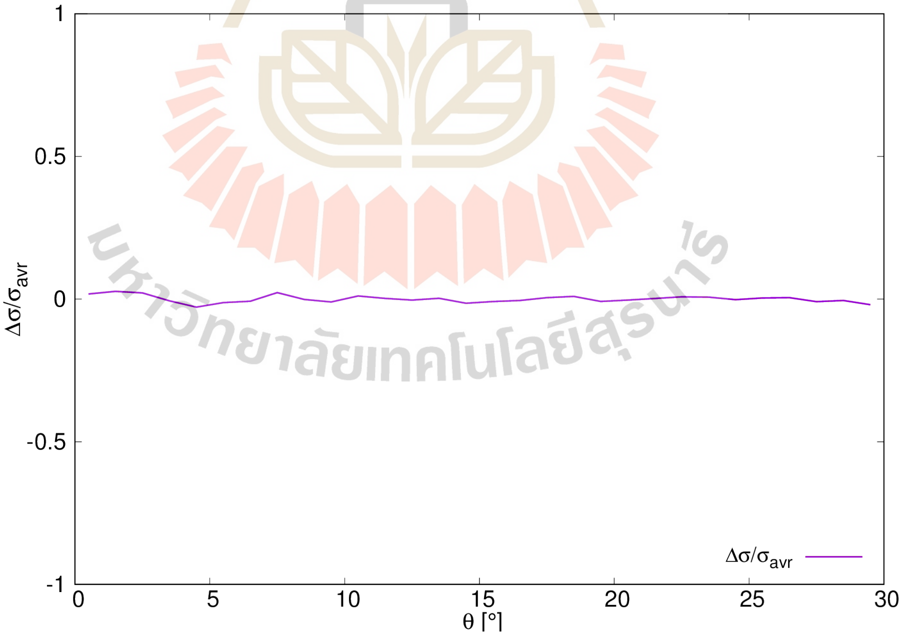

Figure 2.5 Fractional difference of the uncertainties as function of angular bins from 1000 Monte Carlo simulations.

CHAPTER III

SINGLE VOID INTERPRETATION

3.1 ISW Effect From LTB Void

Finelli et al. (2014) calculate the (nonlinear) ISW temperature fluctuations ΔT_{ISW} of LTB void,

$$\Delta T_{\mathrm{ISW}} = -A\left(1 - \frac{28}{13}\frac{\tilde{\theta}^2}{\tilde{\theta}_0^2}\right)e^{-2\frac{\tilde{\theta}^2}{\tilde{\theta}_0^2}} \tag{3.1}$$

where $\tilde{\theta}_0 = \sqrt{3/4\pi}\theta_0$, $\theta_0 = (180^{\mathrm{o}}/\pi)(r_{\mathrm{v}}/D_{\mathrm{d}}(z_0))$ and z_0 is the redshift of void's centre. The unit of θ is degree. The amplitude A is given by

$$A = 148.8\,\mu\mathrm{K}\left(\frac{r_{\mathrm{v}}}{155.3h^{-1}\mathrm{Mpc}}\right)^3\left(\frac{\delta_{\mathrm{c}}}{0.2}\right)^2. \tag{3.2}$$

We can see that these functions need 3 parameters to fit model. The redshift z_0 indicates how far the void is. The size of LTB void r_{v}, and the last parameter the central density contrast δ_{c}.

In order to constrain the super-void to large cold spot of CMB, the $\chi^2_{\mathrm{reduced}}$ method is used to test the goodness of fit,

$$\chi^2_{\mathrm{reduced}} = \frac{\chi^2}{\text{data points} - \text{number of free parameters}}, \tag{3.3a}$$

$$\chi^2 = \Sigma_i \frac{(\Delta T_i^{\mathrm{obs}} - \Delta T_i^{\mathrm{ISW}})^2}{\sigma_i^2}. \tag{3.3b}$$

The best parameter set minimise $\chi^2_{\mathrm{reduced}}$. In principle we expect that the minimum $\chi^2_{\mathrm{reduced}}$ is close to one because if $\chi^2_{\mathrm{reduced}} \ll 1$, it could be refered that our uncertainty σ_i from observational data are overestimated.

Figure 3.1 shows our parameter fitting and the Finelli 2014. The difference between our fitting data process and Finelli et al. (2014) is the error bars of data. While we consider the only the root mean square of fluctuation, Finelli et al. (2014) considers both CMB measurement and LSS survey. The best parameters of our simulation are

$$r_{\mathrm{v}} = 168^{+15}_{-14}\ \mathrm{Mpc}\ h^{-1}, \tag{3.4a}$$

$$z = 0.13^{+0.09}_{-0.05}, \tag{3.4b}$$

$$\delta_{\mathrm{c}} = -0.13^{+0.05}_{-0.05}, \tag{3.4c}$$

$$\chi^2_{\mathrm{reduced}} = 0.98. \tag{3.4d}$$

The χ^2 contour plot between of r_{v} and z with δ_{c} = -0.13 is shown by Figure 3.2. We can see the χ^2 is well constrained withing 1σ region.

3.2 ISW of HSW Void

3.2.1 Newtonian Potential of HSW profile

Before we calculate ISW effect we need to know Newtonian potential. Recall, Poisson's equation of Newtonian potential Φ,

$$\nabla^2_\chi \Phi = \frac{3H_0^2}{2}\Omega_{\mathrm{m}}\frac{\delta}{a}, \tag{3.5}$$

where ∇_χ is the gradient operator with respect to the comoving coordinate χ. Since HSW profile depends only on physical radial r then we can rewritten Eq. 3.5

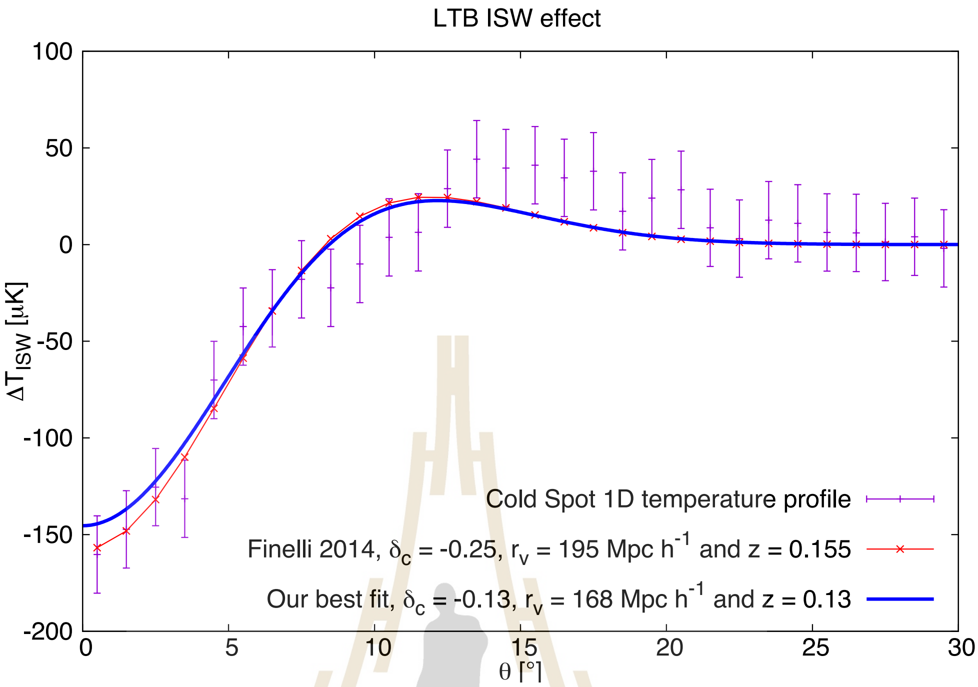

Figure 3.1 LTB void ISW: Blue thick line is the our best parameter set. Red thin line-points is best fit from Finelli 2014 (Finelli et al., 2014).

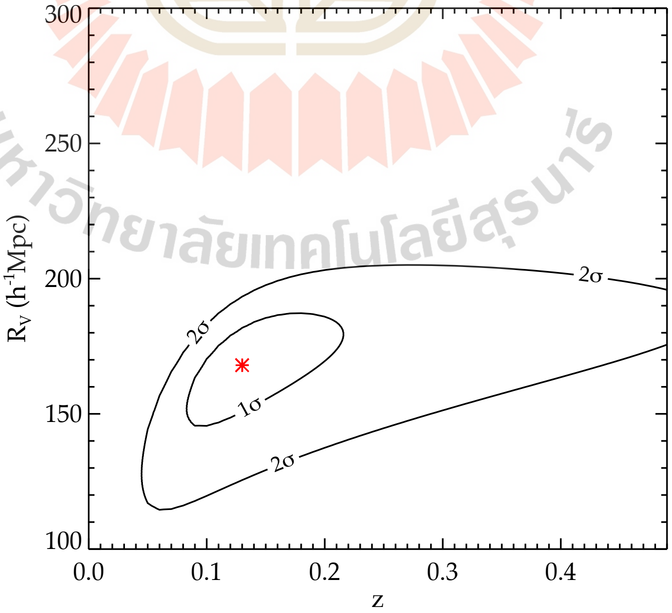

Figure 3.2 χ^2 contour plot between void radius r_v and redshift z with δ_c = -0.13.

as

$$a^2\frac{1}{r^2}\frac{\partial}{\partial r}\left(r^2\frac{\partial\Phi_{\rm H}}{\partial r}\right) = \frac{3H_0^2}{2}\Omega_{\rm m}\frac{\delta_{\rm H}(r)}{a}. \tag{3.6}$$

Or in the form of $x = r/r_{\rm v}$,

$$\frac{1}{x^2}\frac{\partial}{\partial x}\left(x^2\frac{\partial\Phi_{\rm H}}{\partial x}\right) = \frac{3H_0^2\Omega_{\rm m}}{2a^3}r_{\rm v}^2\delta_{\rm H}(x), \tag{3.7}$$

where $\delta_{\rm H}(r)$ is the density contrast of HSW profile (see Eq. 1.28 and 1.31) Now, we can obtain $\Phi_{\rm H}$ by integration

$$\Phi_{\rm H}(r_{\rm v}, x, z = z_0) = \frac{3H_0^2\Omega_{\rm m}}{2a^3}r_{\rm v}^2 \times \tilde{\Phi}_{\rm H}(x), \tag{3.8}$$

where

$$\tilde{\Phi}_{\rm H}(x) = \int_0^x \frac{1}{x'^2}\left[\int_0^{x'} x''^2\delta_{\rm H}(x'')dx''\right]dx'. \tag{3.9}$$

$\Phi_{\rm H}(r_{\rm v}, x, z = z_0)$ is the non redshift (or time) evolution Newtonian potential of HSW profile . For the redshift (or time) evolution form we have,

$$\Phi_{\rm H}(r_{\rm v}, x, z) = D_+(z)\Phi_{\rm H}(r_{\rm v}, x, z = z_0), \tag{3.10}$$

where $D_+(z)$ is linear growth factor normalise to unity at present epoch.

The calculation method and result

Because HSW profile is not an easy function to integrate by analytical symbolic method. Hence we should calculate Eq. 3.9 by numerical method. There are many software library and algorithms for integration such as trapezoidal rule, Newton 3, 5 points methods, Monte Carlo integration, adaptive quadrature integration, etc. In this work we used QAGS routine from GNU Scientific Library (GSL*) which uses adaptive quadrature integration, in computation.

---

*https://www.gnu.org/software/gsl/manual/gsl-ref.pdf

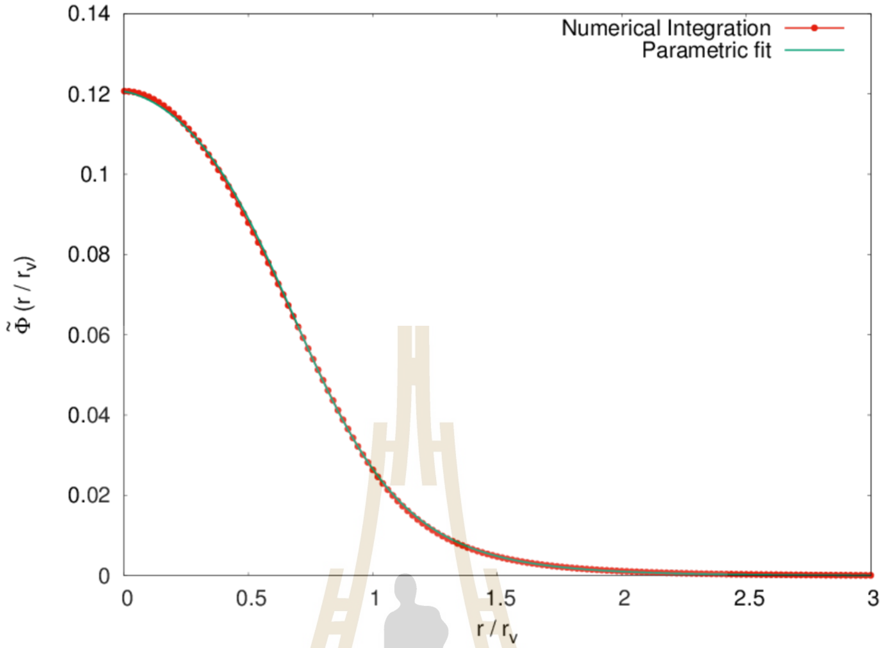

Figure 3.3 The (non-scaled) Newtonian potential from numerical calculation (line with dots) compared to our parametric fitting formula given by Eq. 3.11(green line). We set $r_{\rm s}/r_{\rm v} = 0.91$ (the critical compensate void).

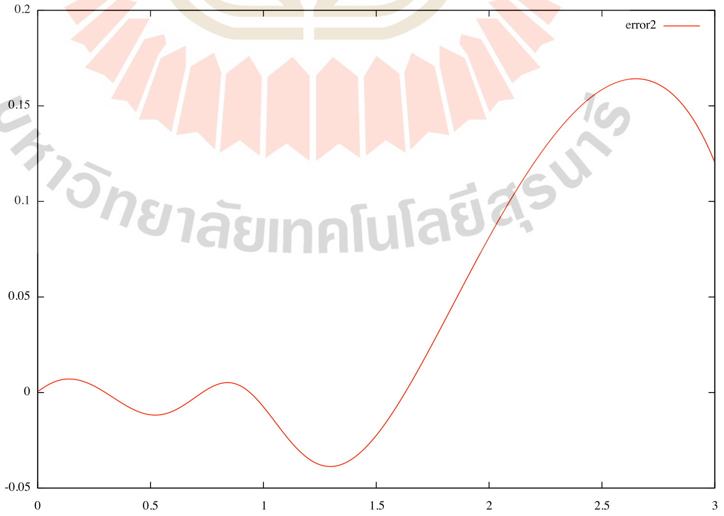

Figure 3.4 The fractional difference $\delta\tilde{\Phi}$ between parametric model and numerical result $\tilde{\Phi}$.

Figure 3.3 is the computational result of non-scale Newtonian potential $\tilde{\Phi}(x)$ in the case which $r_{\mathrm{s}}/r_{\mathrm{v}} = 0.91$. We also create the parametric model

$$\tilde{\Phi}(x) \simeq A(1 + k_0 x^2)^{-1}(1 + k_1 x^4)^{-1} e^{-k_2 x^{2k_3}}, \tag{3.11}$$

where $A = -\delta_{\mathrm{c}} \times 0.1425$, $k_0 = 0.68$, $k_1 = 1.35$, $k_2 = 0.15$ and $k_3 = 0.57$. From Figure 3.3, it is very clear that as r/r_{v} approches to 3 the potential can be neglected. The error of parametric model is illustrated by Figure 3.4.

3.2.2 Ray Tracing Method

The conformal time integral of ISW effect Eq. 1.36 can be written in the form of redshift integral as

$$\frac{\Delta T_{\mathrm{ISW}}(\hat{n})}{\bar{T}} = -\frac{2}{c^2} \int_0^{z_{\mathrm{LS}}} \frac{\partial}{\partial z} \Phi(z, \hat{n}) dz. \tag{3.12}$$

This integration can be discretised into different small redshift slices,

$$\int_0^{z_{\mathrm{LS}}} \frac{\partial}{\partial z} \Phi(z, \hat{n}) dz \to \sum_i \left\{ \Phi(z_{i+1}, \hat{n}) - \Phi(z_{i-1}, \hat{n}) \right\}. \tag{3.13}$$

With linear perturbation density the summation can be described by

$$\sum_i \left\{ \Phi(z_{i+1}, \hat{n}) - \Phi(z_{i-1}, \hat{n}) \right\} = \sum_i D_+(z_i) \left\{ \Phi_0(D_{\mathrm{d}}(z_{i+1}), \hat{n}) - \Phi_0(D_{\mathrm{d}}(z_{i-1}), \hat{n}) \right\}, \tag{3.14}$$

where $\Phi_0(D_{\mathrm{d}}(z), \hat{n})$ is the non-redshift evolution Newtonian potential at the angular diameter distance $D_{\mathrm{d}}(z)$ in direction of $\hat{n}$.

Since D_{d} is nonlinear with z, therefore it is easier to sum over the interval of z in logarithm scale,

$$\log(1 + z_{i+1}) - \log(1 + z_i) = \text{constant}. \tag{3.15}$$

Since we start from $z_0 = 0$ and suppose that an integrand approaches to zero at z_N with N intervals of z. Hence

$$\frac{\log(1+z_N)}{N} = \text{constant}, \tag{3.16}$$

and

$$\log(1+z_i) = i \cdot \frac{\log(1+z_N)}{N}. \tag{3.17}$$

3.2.3 Simulations and Results

HSW profile is density profile for normal void. But in principle we can try to extend the size of void to $r_{\mathrm{v}} > 100$ Mpc h^{-1}. In our simulations, we specify 2300 intervals of redshift z and $z_N = 5$. Initially, we considered 5 parameters to do χ^2 test, the size of void r_{v}, central density contrast δ_{c}, the redshift of centre of void Z_0, α and β of HSW profile. Later on, we found that this is redundant. Since, both α and β relate to r_{s} and r_{s} has more physical meaning than α and β. Consequently, we consider r_{s} instead α and β (see Eq. 1.29 and 1.30).

At first, we use OPENMP to do parallel computing. During that time we found that because for 1 result of 1 parameters set the calculated time is very short (30 second). That means the CPUs did not run with full potential (70 % of CPU's potential). It indicated that we needed to find another way. We switched from OPENMP to parallel summited LINUX script. NARIT's computers cluster was used in this process. Figure 3.5, it is web application interface for monitoring NARIT's computers cluster. The application had shown that the many System Usage of CPU. It means that the calculations are inefficiency because many runtime of CPU loose to system runtime instead calculation runtime. This problem may be caused by GNU Scientific Library (GSL) which is difficult to solve (almost impossible if we still using this library).

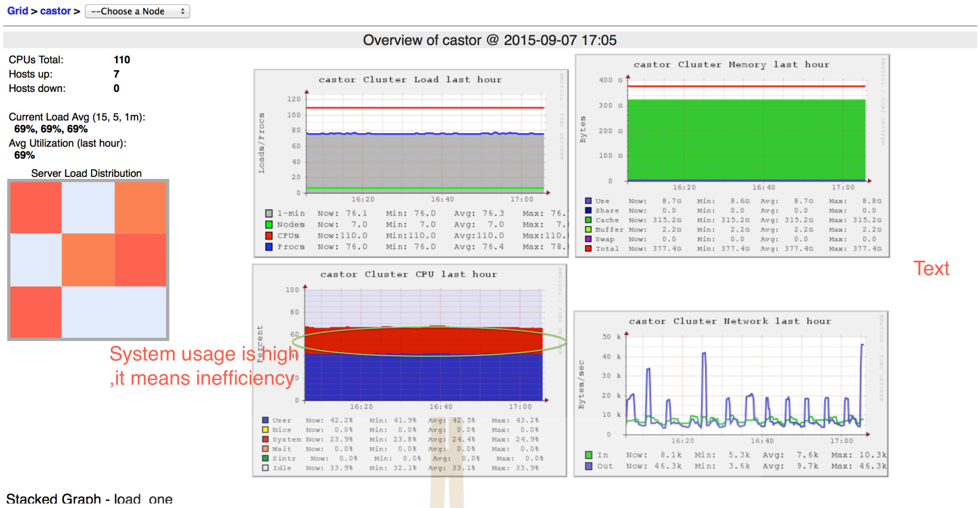

Overview of castor @ 2015-09-07 17:05

CPUs Total: 110
Hosts up: 7
Hosts down: 0

Current Load Avg (15, 5, 1m):
69%, 69%, 69%
Avg Utilization (last hour):
69%

```
1-min  Now: 76.1   Min: 76.0   Avg: 76.3   Max: 76.
Nodes  Now:  7.0   Min:  7.0   Avg:  7.0   Max:  7.
CPUs   Now:110.0   Min:110.0   Avg:110.0   Max:110.
Procs  Now: 76.0   Min: 76.0   Avg: 76.4   Max: 78.
```

```
Use    Now:   8.7G  Min:   8.6G  Avg:   8.7G  Max:   8.8G
Share  Now:   0.0   Min:   0.0   Avg:   0.0   Max:   0.0
Cache  Now: 315.2G  Min: 315.2G  Avg: 315.2G  Max: 315.2G
Buffer Now:   2.2G  Min:   2.2G  Avg:   2.2G  Max:   2.2G
Swap   Now:   0.0   Min:   0.0   Avg:   0.0   Max:   0.0
Total  Now: 377.4G  Min: 377.4G  Avg: 377.4G  Max: 377.4G
```

```
User   Now: 42.2%   Min: 41.9%   Avg: 42.5%   Max: 43.2%
Nice   Now:  0.0%   Min:  0.0%   Avg:  0.0%   Max:  0.0%
System Now: 23.9%   Min: 23.8%   Avg: 24.4%   Max: 24.9%
Wait   Now:  0.0%   Min:  0.0%   Avg:  0.0%   Max:  0.0%
Sintr   Now:  0.0%   Min:  0.0%   Avg:  0.0%   Max:  0.0%
Idle   Now: 33.9%   Min: 32.1%   Avg: 33.1%   Max: 33.9%
```

```
In     Now:  8.1k   Min:  5.3k   Avg:  7.6k   Max: 10.3k
Out    Now: 46.3k   Min:  3.6k   Avg:  9.7k   Max: 46.3k
```

Text

System usage is high ,it means inefficiency

Figure 3.5 NARIT's computer cluster usage.

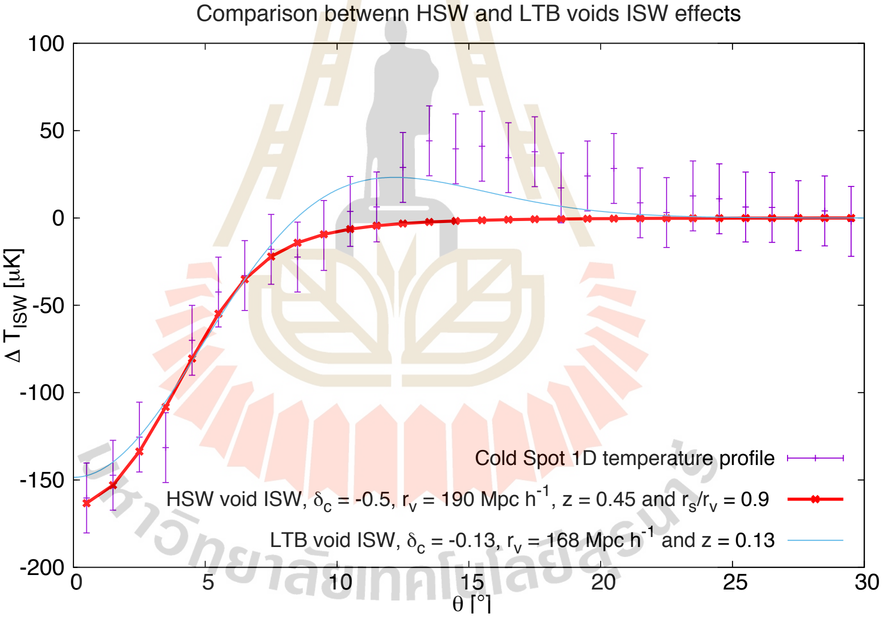

Figure 3.6 Cold spot temperature with ISW fitting: The thick red line is the best fit from HSW void profile. The thin blue line is the best fit from LTB void profile.

Figure 3.6 shows CMB cold spot temperature and ISW effects from LTB and HSW void profiles. For HSW we get best fit parameters $z = 0.45$, $\delta = -0.5$, $r_{\rm v} = 190$ Mpc h^{-1}, $r_{\rm s}/r_{\rm v} = 0.9$ and $\chi^2_{\rm reduced} = 0.99$. We can see that HSW profile approaches zero from negative while Finelli model approaches from positive.

Figure 3.7 shows the contour plot of χ^2 between parameters. We can see that there are correlation between these sets of parameters. In fact, we should specify $\delta_{\mathrm{c}} = -0.5$ and $r_{\mathrm{s}}/r_{\mathrm{v}} = 0.91$ (see Chapter I). If we follow that assumption we find that $r_{\mathrm{v}} = 190^{+20}_{-30}$ Mpc h^{-1} and $z = 0.45^{+0.60}_{-0.13}$ is our best parameters fit.

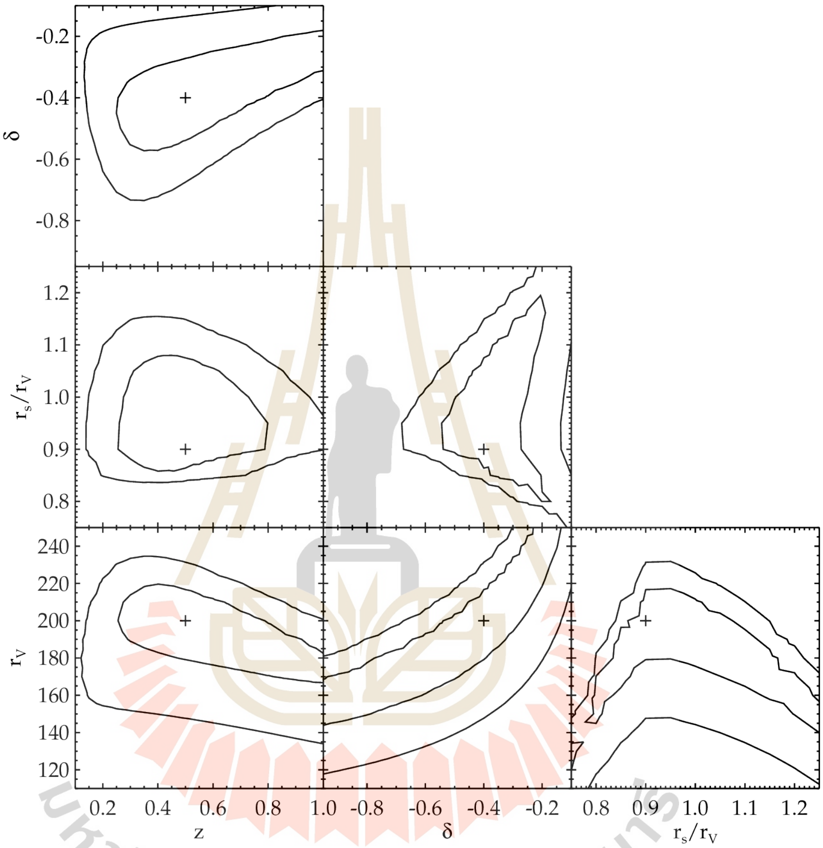

Figure 3.7 Contour plot of χ^2 between parameters.

3.3 Comment on Positive Temperature Fluctuation of Cold Spot

From cold spot temperature profile, there is positive fluctuations from 12 to 15 degree apart from the centre. LTB Finelli et al. (2014) is well fit this positive fluctuation while HSW profile can not give positive fluctuation. However, there are some research such as Nadathur et al. (2014) argue that Finelli et al. (2014) could not explain cold spot. Nadathur et al. (2014) also shown that the positive fluctuation only occur when we consider RS (non-linear ISW) effect but the effect is relatively small when compare to ISW effect. Nadathur et al. (2014) had estimated the RS effect and found that their result is different from Finelli et al. (2014) (see Figure 3.8). In September 2015, (Finelli et al., 2014) reconsidered their model again. The new model becomes more complicated and require parameters more both than the 2014 model and HSW model. For HSW profile ISW we can interpret that we need some overdense region near void to explain the positive fluctuation of this cold spot.

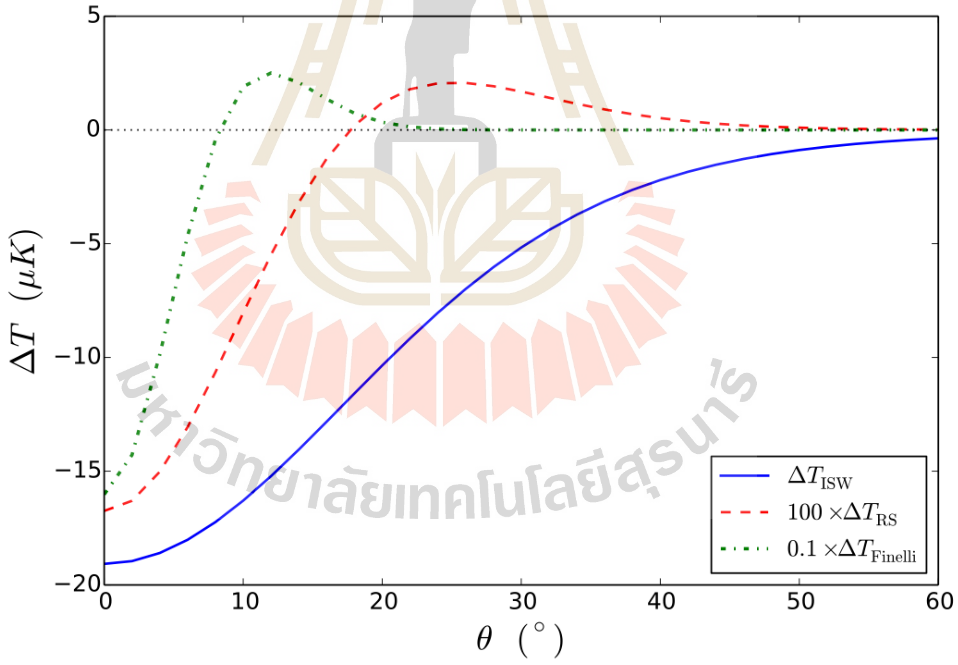

Figure 3.8 The angular dependent of ΔT_{ISW} (blue solid curve) and ΔT_{RS} (red dashed) which are calculated by Nadathur et al. (2014). The RS anisotropy is magnified by a factor of 100 for clarity. The green (dot-dashed) line shows the calculation result of Finelli et al. (2014).

3.4 CMB Weak Gravitational Lensing

In this section we will discuss about detail studying of weak lensing of cosmic void on CMB temperature fluctuation. Lensing potential ψ, deflection angel α, weak lensing induced temperature $\Delta T_{\rm len}$ will be explained in deep.

3.4.1 Lensing Potential

Recall lensing potential formula 1.48 which has speed of light $c = 1$. For the arbitrary unit of c, we have,

$$\psi(\vec{\theta}) = \frac{2}{c^2}\frac{D_{\rm s}}{D_{\rm d}D_{\rm ds}}\int \Phi(\vec{\theta}, \chi)d\chi. \tag{3.18}$$

Chantavat et al. (2016) had find the lensing potential for the effective (HSW) void with parameters $r_{\rm s}/r_{\rm v}$ = 0.91 and δ_c = -0.85.

$$\psi(b/r_{\rm v}, r_{\rm v}, z) \simeq S(r_{\rm v}, z) \times \tilde{\psi}(b/r_{\rm v}), \tag{3.19}$$

where the impact parameter $b = D_d\theta$, $\tilde{\psi}(x)$ is the scale-invariant lensing potential and $S(r_{\rm v}, z)$ is the lensing potential scaling factor.

$$\tilde{\psi}(x) = \psi_0 \exp(\Gamma_0 x^{\gamma_0}) \times (1.0 + x^{\gamma_1})^{\gamma_2}, \tag{3.20}$$

where $\psi_0 = 9.06 \times 10^{-2}$ Mpc^2 h^{-2}, $\gamma_0 = 1.29$, $\gamma_1 = 2.86$, $\gamma_2 = -1.72$ and $\Gamma_0 = -0.31$.

$$S(r_{\rm v}, z) = \frac{16\pi G}{c^2}\Omega_m \rho_{cri}\left(\frac{r_{\rm v}}{\text{Mpc } h^{-1}}\right)^3 \frac{(1+z)^3 D_+(z)}{(D_d/Mpc\, h^{-1})}. \tag{3.21}$$

Note that the growth function $D_+(z)$ indicates that this solution obey the time-evolution of void. This fitting function for the lensing potential is accurate within 10% over the range well within $3r_{\rm v}$ (see Figure 3.9).

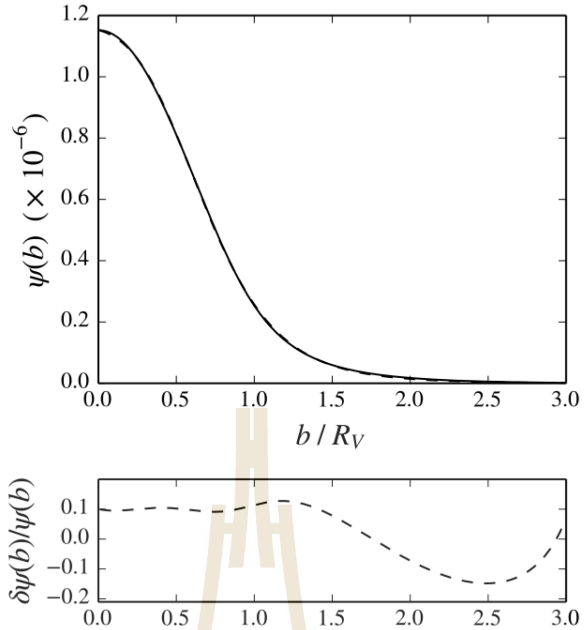

Figure 3.9 Top panel displays the void lensing potential for $r_{\rm v} = 30.0$ Mpc h^{-1} at $z = 0.5$. Bottom panel shows the fractional difference between the anylitical fitting function and the lensing potential calculated numerically. The picture is captured from Chantavat et al. (2016)

3.4.2 Deflection Angle

Let $\xi = b/r_{\rm v}$, now an angular gradient operator ∇_θ becomes,

$$\nabla_\theta = \frac{D_{\rm d}}{r_{\rm v}}\nabla_\xi = \frac{D_{\rm d}}{r_{\rm v}}\left(\frac{\partial}{\partial \xi_i}, \frac{\partial}{\partial \xi_i j}\right), \tag{3.22}$$

where

$$\xi^2 = \xi_i^2 + \xi_j^2, \tag{3.23}$$

and

$$\frac{\partial}{\partial \xi_i} = \frac{\partial \xi}{\partial \xi_i}\frac{\partial}{\partial \xi} = \frac{\xi_i}{\xi}\frac{\partial}{\partial \xi}. \tag{3.24}$$

Now we can take the derivative to ψ to get the deflection angle $\vec{\alpha}$.

$$\vec{\alpha} = \nabla_\theta \psi = S(r_{\rm v}, z)\frac{D_{\rm d}}{r_{\rm v}}\frac{\tilde{\psi}(\xi)}{\xi} \times \left[\Gamma_0 \gamma_0 \xi^{\gamma_0 - 1} - \frac{\gamma_0 \gamma_1 \xi^{\gamma_1 - 1}}{1 + \xi^{\gamma_1}}\right] (\ \xi_i,\ \xi_j). \tag{3.25}$$

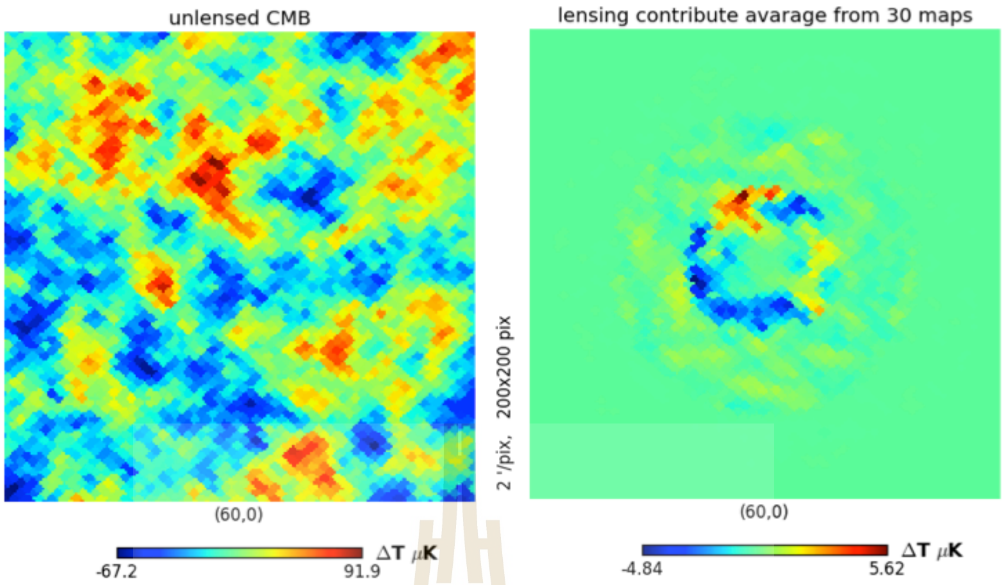

Figure 3.10 Left: The original unlensed CMB fluctuations map in the region of interest. Right: The additional secondary CMB fluctuations caused by weak gravitational lensing from a cosmic void in the foreground.

3.4.3 Weak Lensing CMB temperature

As explained in Chapter 1, weak lensing does not change the temperature of CMB directly but change the photon's paths. So we require the CMB map background to compute the weak lensing temperature. The CMB map can be generated by HEALPix through 'synfast' function. We specify the number of pixels to 12×2048^2 and consider on the area of size 6×6 square of degree. We now, can calculate ΔT_{len} by using Eq. 1.49 and 3.25.

Figure 3.10 shows a secondary CMB fluctuation temperature map due to weak lensing effect. Unlike lensing potential and deflection angle, the pattern of fluctuation is not symmetric due to the non-symmetry in CMB background temperature map. Eq. 1.49 implies that the CMB lensing will strong if the contrast on CMB map is high. Similarly, if the contrast on CMB map low the CMB lensing is also low. As shown by Figure 3.10 the CMB contribution on CMB is relatively

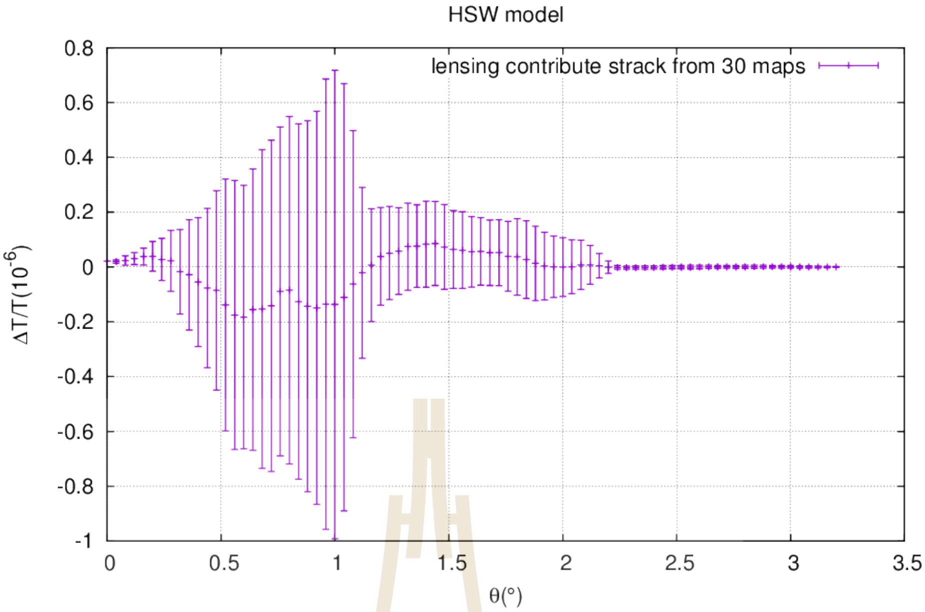

Figure 3.11 The 1D lensing contribution on CMB temperature fluctuation the error bars are the uncertainties of 30 maps stacking.

low to the original CMB due to the smooth of CMB background. The 1D plot Figure 3.11 shows that if we consider only CMB temperature we can not distinguish between either noise or weak lensing contribution. So in studying the cold spot we should ignore the CMB lensing.

CHAPTER IV

MULTIVOID MODEL

4.1 Void Abundance

The origin of CMB cold spot may not be a super-void but the multiple normal size of voids align in local region or in short multi-voids. From previous section, we had illustrated the ray tracing method to calculate ISW effect. In order to apply this method to multi-voids system we need to know exactly where do those voids locate. In principle, we can random voids' locations. But it is very complicate in the implementation process and extreamly computational intensive. So instead of generating the voids' positions randomly we switch to statistical population of cosmic voids approach. Hence, the void abundance is considered. Here, the void abundance is summarised. The reader who want to understand in detail level can follow Pisani et al. (2015). The abundance of voids can be described by

$$\frac{M^2 n(M,z)}{\bar{\rho}}\frac{dM}{M} = \nu f(\nu)\frac{d\nu}{\nu}, \tag{4.1}$$

where M is the void mass, $\bar{\rho}$ the background density, and $n(M,z)$ the number density of voids of given mass and redshift. The fraction $f(\nu)$ of mass that has evolved into voids can be approximated as:

$$\nu f(\nu) \approx \sqrt{\frac{\nu}{2\pi}}\exp(-\nu/2), \tag{4.2}$$

where $\nu = \frac{\delta_\nu^2}{\sigma^2(M)}$, δ_ν is the critical underdensity of void formation and $\sigma^2(M)$ is the variance of linear density fluctuations on a scale $R = (\frac{3M}{4\pi\bar{\rho}})^{-1/3}$. The variance of linear density fluctuations can be calculated by

$$\sigma^2(M) = \frac{1}{2\pi^2}\int^{\infty} k^2 P(k) w(kr)^2 dk, \tag{4.3}$$

where $P(k)$ is the linear power spectrum of density perturbations and $w(kr)$ is the windows function, given by

$$w(kr) = 3\frac{\sin(kr) - kr\cos(kr)}{(kr)^3}, \tag{4.4}$$

where, k is the comoving wave number. In linear Cold Dark Matter (CDM) model the power spectrum can be written as

$$P(k, z) \propto k^n T^2(k) D_+^2(z), \tag{4.5}$$

where $T(k)$ is the transfer function which can be solving Einsteien-Boltzmann equation. Software library such as 'CosmoloPy'* can be used to calculate both the variance of density fluctuations $\sigma^2(M)$ and $P(k, z)$. From Pisani et al. (2015), indicates that the appropriate value of δ_ν is -0.45. Note that this number density $n(M, z)$ only tells us how many voids are in the given volume $V(z)$. It dose not tell how voids distribute within the volume. From Eq. 4.1 we can calculate the expected number of void in redshift range z to $z + \Delta z$ with the radii range R to $R + \Delta R$ as:

$$N = \int_z^{z+\Delta z} dz \int_R^{R+\Delta R} dR \int_\Omega n(R, z) d\Omega \frac{dV}{dzd\Omega} \tag{4.6}$$

where dV is the comoving volume element and the angular integration is over the angular size of the consideration. From Eq. 4.1 and 4.6, it is clear that the number of voids depend on the cosmological model through σ and the differential volume element.

---

*http://roban.github.io/CosmoloPy/

4.2 The Probability of Findding A Super-Void

Consider ΛCDM cosmology with cosmological parameters $\Omega_\Lambda = 0.7$, $\Omega_m = 0.3$ and $h = 1$, we can use Eq. 4.1 and 4.6 to find the density over $0.05 < z < 5$ region with minimum radii of void $R_{\mathrm{v}}^{\mathrm{min}}$. Figure 4.1 illustrate the void abundance where the integration in Eq. 4.6 is performed from $R_{\mathrm{v}}^{\mathrm{min}}$ to 1000 Mpc h^{-1}. From the plot we can see that the number density of void decrease when the radius increase.

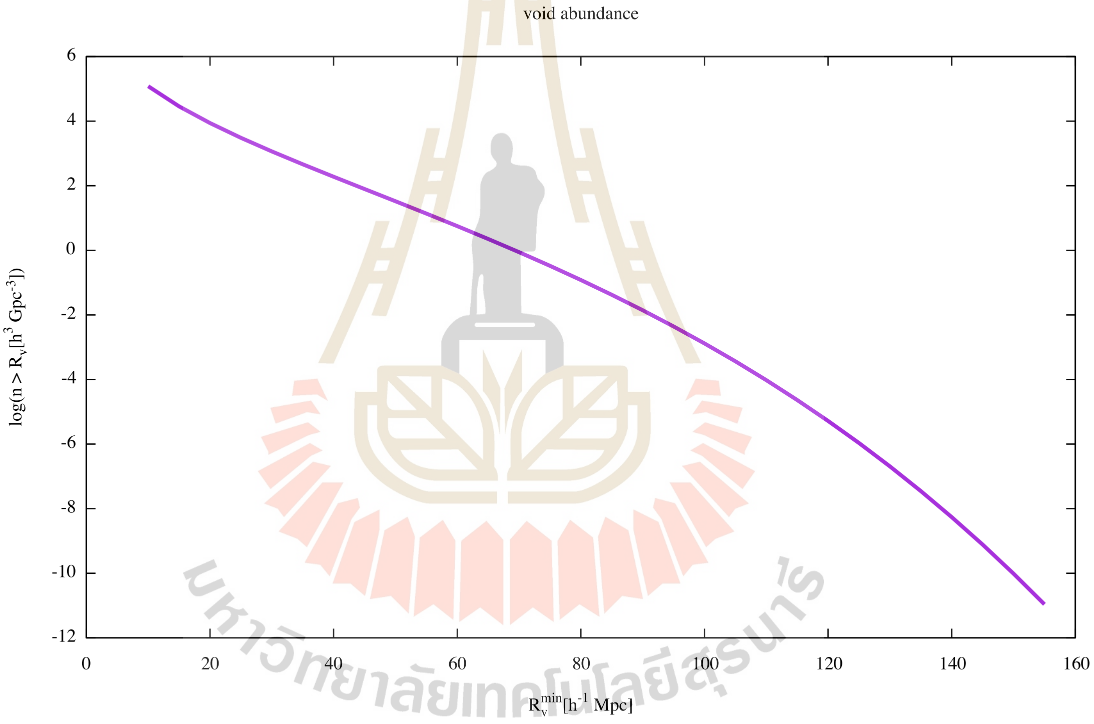

Figure 4.1 The plot between logarithm of number density n in the unit volume (Mpc^3 h^{-3}) and the minimum radii $R_{\mathrm{v}}^{\mathrm{min}}$ of consideration.

In the previous chapter, we had shown that the best-fit radius of HSW profile to CMB cold spot anomaly is $r_{\mathrm{v}} = 190$ Mpc h^{-1}. We can calculate the probability to find such void of size by find the ratio between number of void of size greater than 150 and 10 Mpc h^{-1}, respectively.

$$\mathrm{P}(r_{\mathrm{v}} \geqslant 150 \text{ Mpc } h^{-1}) = \frac{n(R_{\mathrm{v}}^{\mathrm{min}} = 150 \text{ [Mpc } h^{-1}])}{n(R_{\mathrm{v}}^{\mathrm{min}} = 10 \text{ [Mpc } h^{-1}])}. \tag{4.7}$$

By using Eq. 4.7 we find that $\mathrm{P}(150 \text{ Mpc } h^{-1}) \approx 10^{-16}$. This very small probability means that if we believe in ΛCDM and the void abundance theory correct, the super-void is unlikely. On the other hands, ΛCDM model may need to be verified. However, if the ΛCDM model is correct and such a super-void does exist, we may need to invoke the multiverse cosmology. In multiverse cosmology, we can interpret the small probability to find the super-void as there should be at least 10^{16} local-Universes to ensure that the super-void really exists. And it is just coincidental that our Universe has one of this super void.

4.3 ISW of Multiple Voids Along The Same Line of Sight

The ray tracing method require the well known position of each void. But our number density only tell us how many voids in the volume. Hence, for simplicity, we may assume that all of voids' centre align in the same direction by considering the sky area 5×5 square degree. In addition we also consider that all voids have the same effective radius r_{eff} and the same central density contrast δ_{c}. The effective radius r_{eff} can be evaluated by

$$r_{\mathrm{eff}} = \frac{\int_0^\infty dz \int_{R_{\mathrm{v}}^{\mathrm{min}}}^\infty R dR \int_\Omega n(R,z) d\Omega \frac{dV}{dz d\Omega}}{\int_0^\infty dz \int_{R_{\mathrm{v}}^{\mathrm{min}}}^\infty dR \int_\Omega n(R,z) d\Omega \frac{dV}{dz d\Omega}}. \tag{4.8}$$

Note that this effective radius r_{eff} is sensitive to the minimum radius of void $R_{\mathrm{v}}^{\mathrm{min}}$ that we consider. We define density weight function $\tilde{n}(z, R_{\mathrm{v}}^{\mathrm{min}})$ by

$$\tilde{n}(z, R_{\mathrm{v}}^{\mathrm{min}}) = \int_{R_{\mathrm{v}}^{\mathrm{min}}}^\infty dR \int_\Omega n(R,z) d\Omega \frac{dV}{dz d\Omega}. \tag{4.9}$$

Now if we have voids of radius r_{eff} locate at z_0 with the potential $\Phi(z, z_0, \theta)$, the ISW effect of these voids will be given by

$$\frac{\Delta T_{\text{ISW}}(\theta)}{\bar{T}} = -\frac{2}{c^2}\int_0^{z_{\text{LS}}} \tilde{n}(z_0, R_{\text{v}}^{\text{min}})dz_0 \int_0^{z_{\text{LS}}} dz\frac{\partial\Phi(z, z_0, \theta)}{\partial z}. \tag{4.10}$$

The integration with respect to z is just the ISW for a single void, while the integration with respect to z_0 is the integration of ISW from all of void with density weight function $\tilde{n}(z_0, R_{\text{v}}^{\text{min}})$.

4.3.1 Calculations

In the simulations the scale radius to void characteristic radius ration $r_{\text{s}}/r_{\text{v}}$ is specified to be 0.91. As a consequent, it means that the Newtonian potential in simulations is well defined by Eq. 3.11. Our free parameters are central density contrast δ_{c} and the minimum radius of void $R_{\text{v}}^{\text{min}}$. Initially, we had used GSL to integrate Eq. 4.10 but we found that there was a problem with the boundary of integration. Later on, GSL-QAGS function was gave up and replaced by Simpson's rule method.

Figure 4.2 illustrates the ISW effect of multiple voids with minimum radius 10 Mpc h^{-1} and central density contrast -0.6 in the same line of sight. We can see that ISW profile is very similar to negative Dirac delta function. This happen because for a single void the ISW fluctuation approaches to zero when $r/r_{\text{v}} > 3$ and when we add ISW effect from many voids in the same line of sight obviously, the result should be similar to top-hat (or delta) function. We can conclude that the multiple voids in the same line of sight could not be used to describe the origin of CMB cold spot anomaly. So we need the multiple voids model that all voids' centre do not share the same line of sight. Besides, such configuration very unlikely to happen in nature.

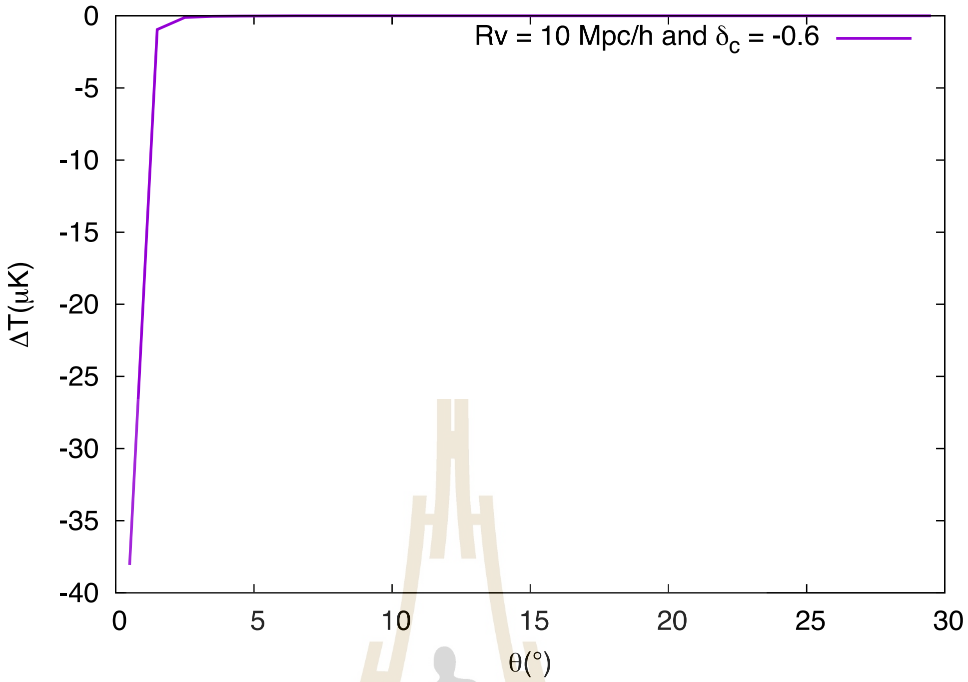

Figure 4.2 The plot between the ISW induced temperature $\Delta T_{\rm ISW}$ of multiple void align in the same line of sight and the angular radius, the fluctuation profile look like negative delta function. All voids are supposed to be the same.

4.4 Multi-Voids Align in Different Lines of Sight

From previous section we can see that the model of multiple voids align in the same line of sight fail in describe the origin of CMB cold spot anomaly. It require the model which voids' centre align in different lines of sight. When we consider Figure 4.2, it is obvious that the ISW profile is very similar to negative Dirac delta function. The cold spot temperature profile (see Figure 2.4) also look like negative Gaussian function. Following that consideration, if we make a assumption that voids locate in the perpendicular line of sight by the 2D normal distribution.

$$F_{\perp}(\phi_x, \phi_y) = A\exp(-(\phi_x^2 + \phi_y^2)/\sigma^2), \tag{4.11}$$

where A is the multiple factor of voids number to satisfy the peak decrement temperature of cold spot. Therefore, the ISW temperature fluctuations at any given point θ in the sky has contributions from multiple voids locate at various (ϕ_x, ϕ_y) can be given by

$$\Delta T_{\rm ISW}(\theta) = \int_{\phi} d^2\phi \; F_{\perp}(\phi_x, \phi_y) \; \Delta\tilde{T}(\theta, \phi_x, \phi_y). \tag{4.12}$$

where $T(\theta, \tilde{\phi}_x, \phi_y)$ is the ISW contributions from voids located at (ϕ_x, ϕ_y). Note that this equation can be applied to any kind of distribution $F_{\perp}(\phi_x, \phi_y)$, in our case $F_{\perp}(\phi_x, \phi_y)$ is defined by Eq. 4.11, the normal distribution. Since our distribution is spherically symmetry, the 2D-integration Eq. 4.12 can be calculated by

$$\Delta T_{\rm ISW}(\theta) = 2\pi \int_{\phi} \phi d\phi \; F_{\perp}(\phi) \; \Delta\tilde{T}(\theta, \phi), \tag{4.13}$$

where $\phi^2 = \phi_x^2 + \phi_y^2$. Again, we can estimate Eq. 4.13 by transform to a summation,

$$\Delta T_{\rm ISW}(\theta) \simeq 2\pi \sum_i \left\{ \frac{1}{2} [F_{\perp}(\phi_{i+1})\phi_{i+1} + F_{\perp}(\phi_{i-1})\phi_{i-1}] \times \Delta\tilde{T}(\theta, \phi_i) \right\}. \tag{4.14}$$

Now the total number of void $N_{\rm total}$ will be

$$N_{\rm total} = 2\pi \int_0^{\infty} \phi d\phi F_{\perp}(\phi) N_{\Omega}, \tag{4.15}$$

where N_{Ω} is given by Eq. 4.6 with the solid angle $\Delta\Omega$. Because N_{Ω} does not depend on ϕ, then, for our $F_{\perp}(\phi)$ (see Eq. 4.11) Eq. 4.15 will be

$$N_{\rm total} = 2A\pi\sigma^2 \times N_{\Omega} \tag{4.16}$$

4.4.1 χ^2 Test

We can do the χ^2 test of fitting CMB cold spot with multi-voids model by using Eq. 4.14. Reminding that, we have four free parameters, the central density contrast δ_{c}, the minimum radius $R_{\mathrm{v}}^{\mathrm{min}}$, the multiplie A (see Eq. 4.11) and the uncertainty of re-distributed voids on redshift plane σ. In this process we had considered ranges of parameter :

$$
\begin{aligned}
5 \leqslant R_{\mathrm{v}}^{\mathrm{min}} \leqslant 30 \quad [\mathrm{Mpc}\, h^{-1}],\\
-0.9 \leqslant \delta_{\mathrm{c}} \leqslant -0.2,\\
0 \leqslant A \leqslant 12,\\
1 \leqslant \sigma \leqslant 5.5, \quad [^{\circ}].
\end{aligned}
$$

Figure 4.3 illustrates comparison between ISW temperature anisotropy (purple

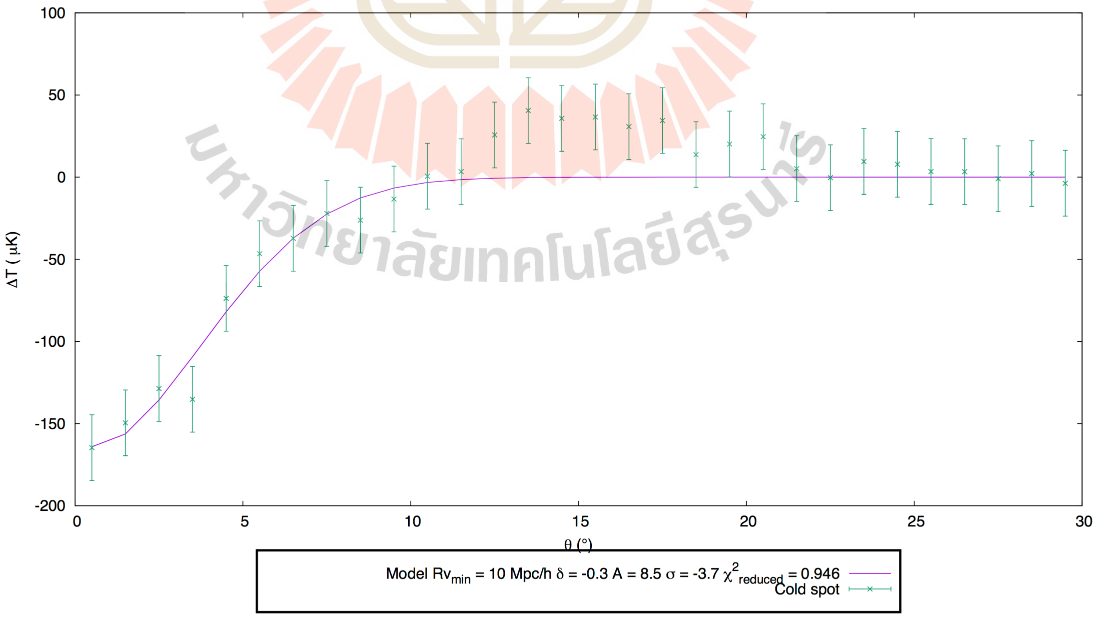

Figure 4.3 The plot between ISW temperature fluctuation of the best fit parameters set and CMB cold spot temperature profile.

solid line) of the best parameters set and the cold spot temperature profile. The best fit parameters are :

$$\delta_{\rm c} = -0.3 \ ,$$

$$R_{\rm v}^{\rm min} = 10 \ {\rm Mpc} \ h^{-1} \ ,$$

$$A = 8.5 \ ,$$

$$\sigma = 3.7 \ ,$$

$$\chi^2_{\rm reduced} = 0.946 \ .$$

If we consider only $\chi^2_{\rm reduced}$ of the best fit parameters set, the model seems very promising. However the modelling without uncertainty is meaningless. Again, we used $\chi^2_{\rm reduced}$ contour plot to constrained the uncertainty of multi-voids align in different lines of sight [with normal distribution] model. Figure 4.4 shows that there are two local minima when we hold A and σ fix as their best fit values. Figure 4.5, 4.6, 4.7 and 4.8 illustrate a good constraint of our parameters. However many local minimum points are showed by contour plot between $\delta_{\rm c}$ and A. This means A correlates to $\delta_{\rm c}$. Consequently, we need to specify either $\delta_{\rm c}$ or A. It is the parameter that how many voids that we represent in the model, the higher A is, the higher number of voids will be. The higher number of voids means the lower of temperature fluctuation. While the lower $\delta_{\rm c}$ leads to colder fluctuation. Fortunately, we can use nonlinear relationship between $\delta_{\rm c}$ and $r_{\rm v}$ which is implied by Figure 1.8 (see Hamaus et al. (2014)).

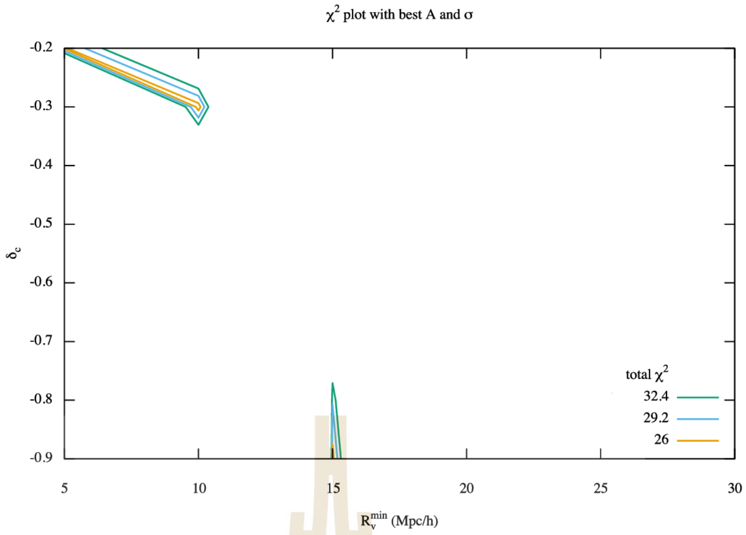

Figure 4.4 χ^2 contour plot between $R_{\mathrm{v}}^{\mathrm{min}}$ and δ_{c} with best fit of A and σ. The χ^2 values 26, 29.2 and 32.4 represent 1σ, 3σ and 5σ standard deviation respectively. The uncertainty σ can be found by plot contour line that χ^2 value equal to the number of degree of freedom (Press et al., 2007).

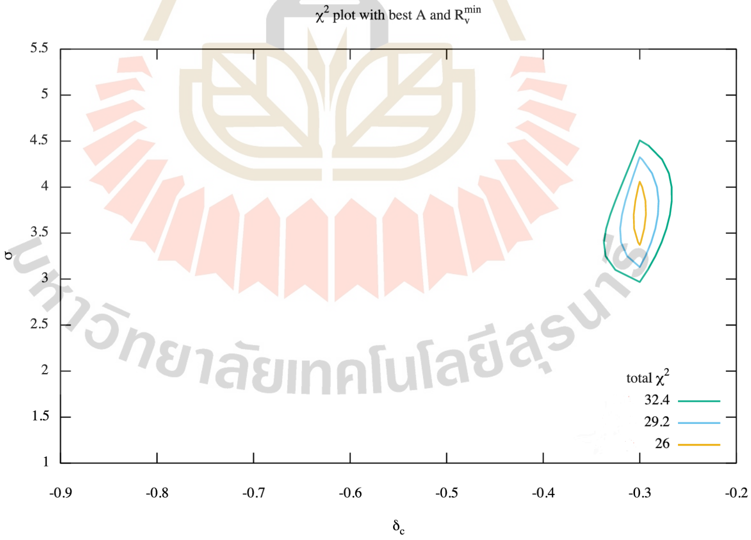

Figure 4.5 χ^2 contour plot between σ and δ_{c} with best fit of A and $R_{\mathrm{v}}^{\mathrm{min}}$. The χ^2 values 26, 29.2 and 32.4 represent 1σ, 3σ and 5σ standard deviation respectively. The uncertainty σ can be found by plot contour line that χ^2 value equal to the number of degree of freedom (Press et al., 2007).

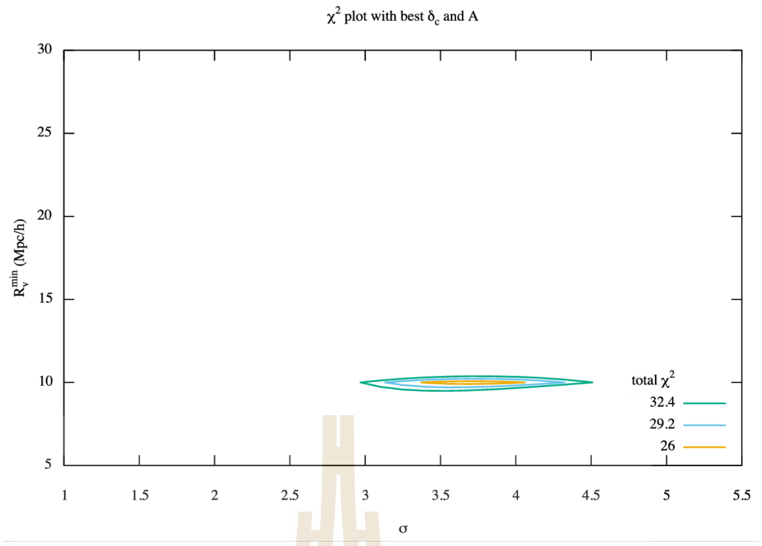

Figure 4.6 χ^2 contour plot between σ and $R_{\rm v}^{\rm min}$ with best fit of $\delta_{\rm c}$ and A. The χ^2 values 26, 29.2 and 32.4 represent 1σ, 3σ and 5σ standard deviation respectively. The uncertainty σ can be found by plot contour line that χ^2 value equal to the number of degree of freedom (Press et al., 2007).

4.4.2 Reducing Degeneracy Using $\delta_{\rm c}$ and $r_{\rm v}$ Relationship

From Figure 1.8 in chapter I, there is relationship between $\delta_{\rm c}$ and $r_{\rm v}$. This relationship can help us to reduce the degeneracy between A and δ_c seen in Figure 4.9.

$$\delta_{\rm c} = \begin{cases} -0.0001r_{\rm v}^2 + 0.0174r_{\rm v} - 1.03, & 5 < r_{\rm v} < 75 \text{ Mpc } h^{-1} \\ -0.5, & r_{\rm v} < 75 \text{ Mpc } h^{-1}. \end{cases} \tag{4.17}$$

This time our number of free parameters reduces to 3, $R_{\rm v}^{\rm min}$, A and σ. We still need to know $\delta_{\rm c}$ average $\bar{\delta}_c$ by:

$$\bar{\delta}_c = \frac{\int_0^\infty dz \int_{R_{\rm v}^{\rm min}}^\infty \delta_{\rm c}(R) dR \int_\Omega n(R,z) d\Omega \frac{dV}{dz d\Omega}}{\int_0^\infty dz \int_{R_{\rm v}^{\rm min}}^\infty dR \int_\Omega n(R,z) d\Omega \frac{dV}{dz d\Omega}}. \tag{4.18}$$

From previous result we found that there is degeneracy between $\delta_{\rm c}$ and A. Now $\delta_{\rm c}$ is a function of $r_{\rm v}$. Therefore, we expect that there would remains some correla-

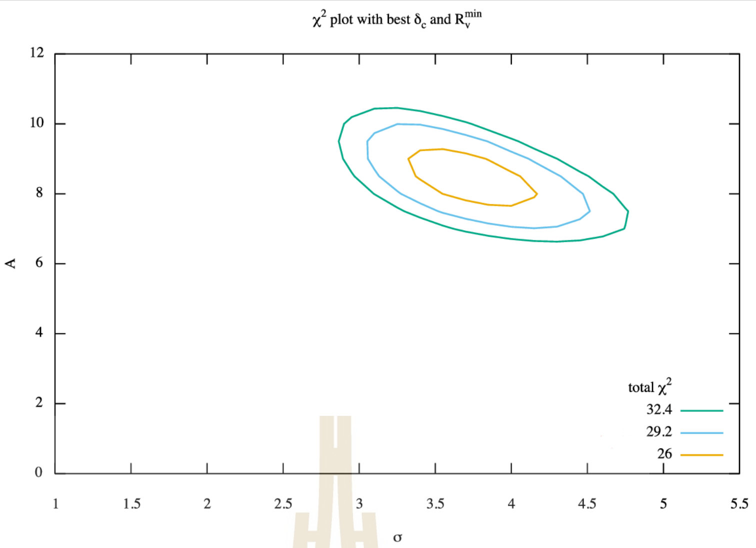

Figure 4.7 χ^2 contour plot between σ and A with best fit of δ_c and R_v^{min}. The χ^2 values 26, 29.2 and 32.4 represent 1σ, 3σ and 5σ standard deviation respectively. The uncertainty σ can be found by plot contour line that χ^2 value equal to the number of degree of freedom (Press et al., 2007).

tions between R_v^{min} and A. With the effective $\bar{\delta}_c$, the best fit parameters set now becomes,

$$R_v^{\mathrm{min}} = 5^{+2}_{-0} \text{ Mpc } h^{-1} , \tag{4.19a}$$

$$A = 1.75^{+0.25}_{-0.25} , \tag{4.19b}$$

$$\sigma = 3.7^{+0.3}_{-0.3} , \tag{4.19c}$$

$$\chi^2_{\mathrm{reduced}} = 0.938 . \tag{4.19d}$$

As we expect, there is small correlation between R_v^{min} and A as showed by Figure 4.12. With $A = 1.75$, the number of voids will be 36283025. If we consider the fact that the normal distribution approaches zero as $\phi \to 3\sigma$, it means that we consider voids in the area of $\approx (3\sigma)^2$ on the sky. The number of voids in such

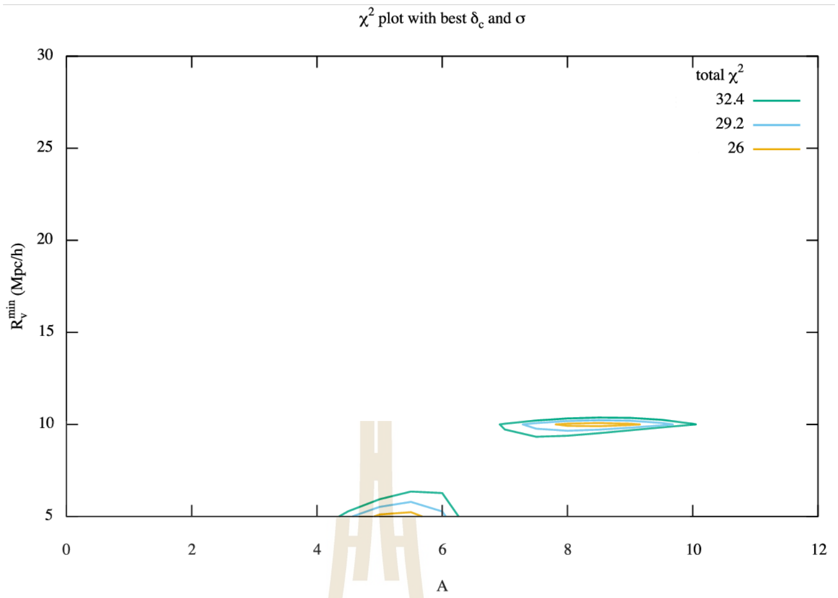

Figure 4.8 χ^2 contour plot between A and $R_{\mathrm{v}}^{\mathrm{min}}$ with best fit of δ_{c} and σ. The χ^2 values 26, 29.2 and 32.4 represent 1σ, 3σ and 5σ standard deviation respectively. The uncertainty σ can be found by plot contour line that χ^2 value equal to the number of degree of freedom (Press et al., 2007).

volume ($\sigma = 3.6°$) given by the standard LSS formation theory (see Eq. 4.1) is 4800000. Hence, to fit the cold spot it requires the number of voids 7.6 times the number from standard LSS formation theory.

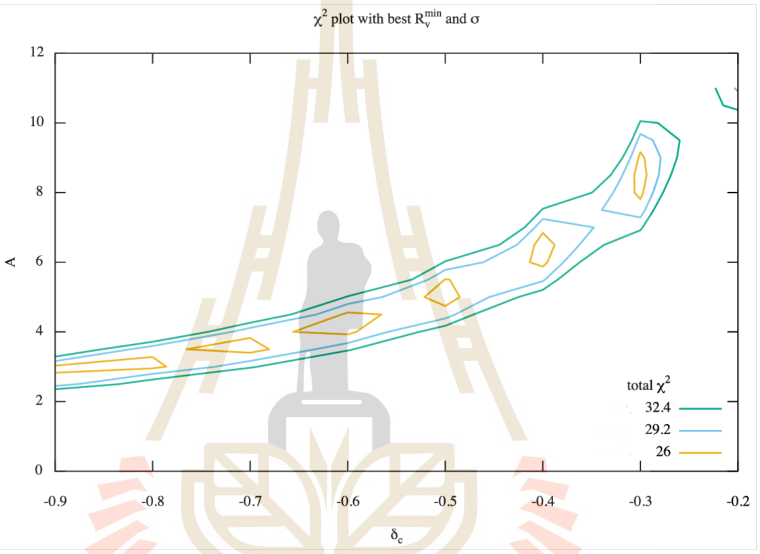

Figure 4.9 χ^2 contour plot between δ_c and A with best fit of $R_\mathrm{v}^\mathrm{min}$ and σ. The χ^2 values 26, 29.2 and 32.4 represent 1σ, 3σ and 5σ standard deviation respectively.The uncertainty σ can be found by plot contour line that χ^2 value equal to the number of degree of freedom (Press et al., 2007).

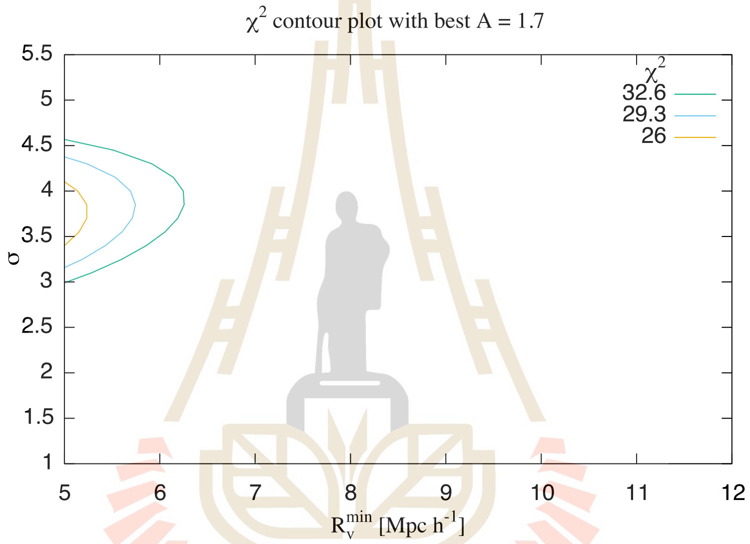

Figure 4.10 χ^2 contour plot between σ and $R_{\mathrm{v}}^{\mathrm{min}}$ with best fit of A. The χ^2 values 26, 29.3 and 32.6 represent 1σ, 3σ and 5σ standard deviation respectively. The uncertainty σ can be found by plot contour line that χ^2 value equal to the number of degree of freedom (Press et al., 2007).

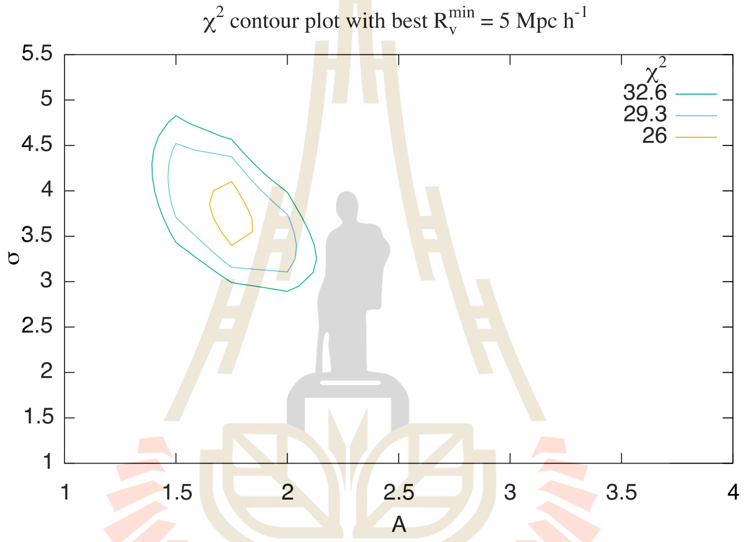

Figure 4.11 χ^2 contour plot between A and σ with best fit of $R_{\rm v}^{\rm min}$. The χ^2 values 26, 29.3 and 32.6 represent 1σ, 3σ and 5σ standard deviation respectively.The uncertainty σ can be found by plot contour line that χ^2 value equal to the number of degree of freedom (Press et al., 2007).

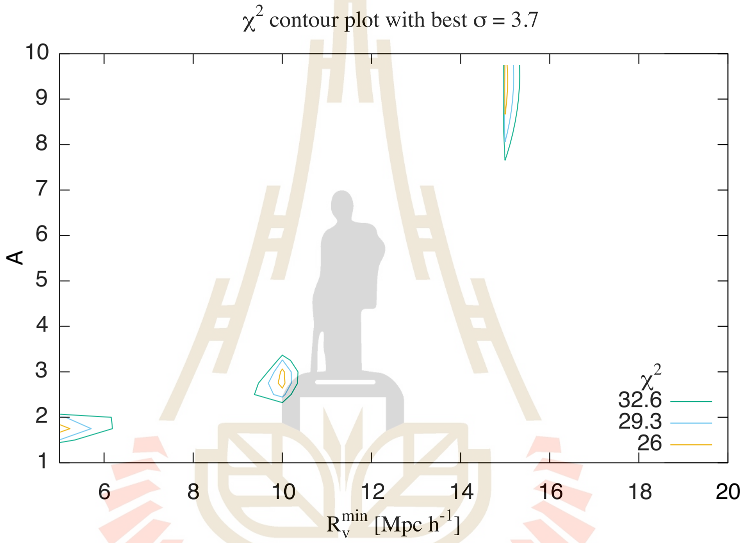

Figure 4.12 χ^2 contour plot between $R_v^{\min}$ and A with best fit of σ. The χ^2 values 26, 29.3 and 32.6 represent 1σ, 3σ and 5σ standard deviation respectively.The uncertainty σ can be found by plot contour line that χ^2 value equal to the number of degree of freedom (Press et al., 2007).

CHAPTER V

CONCLUSION

5.1 Summary of The Main Results

In this thesis, we aim to investigate one of the unsolved problem in modern cosmology, namely the origin of CMB cold spot anomaly. In chapter I, we had reviewed requirement knowledge cosmological theory and its observation support evidence such as CMB, Type Ia supernovae etc. The WMAP's CMB experiments had shown that there is some anomaly results such as the large cold spot which has ten times lower than temperature fluctuation and approximately10 degree angular radius on the sky. Since this structure can not be combinated by ΛCDM framework, thus, the origin of CMB cold spot need to be investigated. Since the origin of the cold spot is not expected from primordial CMB anisotropy fluctuations, then we aim to study CMB cold spot as secondary CMB fluctuations. For the large scale, the secondary CMB anisotropy fluctuations could be cause by the late time ISW effect, RS, SZ or weak gravitational lensing effect. In this thesis we only consider the effects from ISW and weak lensing. The source of ISW effect should be the cosmic void, the underdense structure. Throughout the thesis, we consider 3 models of cosmic voids. The first one is called LTB. The second is HSW. Both LTB and HSW models are treat as the single super-void. The last is multiple voids model which is considered as the multiple normal size of HSW voids align in the considered cosmic volume.

In chapter II, the data from Planck satellite was discussed. We used data from SMICA pipeline which covers frequency range from 30 to 857 GHz in nine frequency bands and has maximum angular resolution up to $l_{\mathrm{max}} = 4000$. We had demonstrated the data analysis method for obtaining 1D CMB cold spot temperature profile. The Fits file from SMICA was read by HEALpix python (Healpy). The 1D temperature profile can be calculated by average the temperature of pixel indices inside the rings of consideration. After measure data, we found that the CMB cold spot anomaly has 1D temperature profile very similar to negative Gaussian function with some positive value of fluctuation (see Figure 2.4). The error bar of cold spot profile is the normal uncertainty of CMB fluctuation (18 μK) plus the instrument noise (2 μK). From Figure 2.4, we can see that the angular radius of the cold spot is not just 10 degree but can be considered as 20 degree.

In chapter III, we modelled a single super void as the origin of CMB cold spot anomaly. For LTB model, we used nonlinear ISW (or RS) effect (see Eq. 3.1) which proposed by (Finelli et al., 2014), to constrain LTB void parameters with the cold spot 1D temperature profile. We found that the best fit parameters set for LTB is the central density contrast $\delta_{\mathrm{c}} = -0.13^{+0.05}_{-0.05}$, the radius of void $r_{\mathrm{v}} = 168^{+15}_{-14}$ Mpc h^{-1} and the redshift of void $z = 0.13^{+0.09}_{-0.05}$ with the goodness of fit $\chi^2_{\mathrm{reduced}} = 0.98$. After that we calculate the ISW effect for HSW model by using ray tracing method. HSW model gives us the best fit parameter set, $\delta_{\mathrm{c}} =$ -0.5 (specific value), the scale radius $r_{\mathrm{s}}/r_{\mathrm{v}} = 0.91$, $r_{\mathrm{v}} = 190^{+20}_{-30}$ Mpc h^{-1} and $z = 0.45^{+0.60}_{-0.13}$ with the goodness of fit $\chi^2_{\mathrm{reduced}} = 0.99$. In addition to ISW effect, we discussed about weak gravitational lensing effect. Because the weak gravitational lensing does not change the temperature of photon, but it change the trajectory of photon. Hence, the weak gravitational lensing can change the appearance of CMB map. This means the weak gravitational lensing effect is background dependent effect. If the CMB map background has low contrast the weak lensing contribution will end up as insignificant. As ΛCDM states that, on large scale the Universe is said to be smooth that means low cosmic variance, consequently we expect negligible effect from weak gravitational lensing as illustrated by Figure 3.11. So we can conclude that in both a super void and multiple voids models weak gravitational lensing can be ignored.

In chapter IV, the ISW effect of multiple voids had been calculated. Firstly, we considered the number density of void as a function of size and redshift by work of Pisani et al. (2015). We found that for the void of radius greater than 150 Mpc h^{-1}, the probability to find such void is roughly 10^{-16}. In the simulation we used statistical approach to calculate the ISW effect from multiple voids. For simplicity, we made the assumption that all voids have the same size, same central density contrast and same line of sight. Later on we found that this assumption led us to ISW temperature profile like negative delta function (see Figure 4.2). We add another assumption that there is a correlation of voids across red shift bins such a way that the number of voids in the direction perpendicular to line of sight are normally distributed (see Eq. 4.11, 4.12 and 4.13). This adding assumption give better goodness of fit $\chi^2_{\mathrm{reduced}}$. But because the high degenracy between parameter A and the minimum radius of voids δ_{c}, we reconsider the fitting process by adding the relationship between the central density contrast δ_{c} and void's radius r_{v} (see Eq. 4.17). This time we obtained the well constrained of multiple voids model with the best fit parameters set, $R_{\mathrm{v}}^{\mathrm{min}} = 5^{+2}_{-0}$ Mpc h^{-1} , $A = 1.75^{+0.25}_{-0.25}$, $\sigma = 3.7^{+0.3}_{-0.3}$ and the goodness of fit $\chi^2_{\mathrm{reduced}} = 0.938$. It corresponds to 36283025 number of voids which 7.6 times value of standard LSS formation theory. This result shows that the super void model is not the unique solution of the origin of CMB cold spot anomaly.

Table 5.1 Summary of best fit parameters.

Model	$r_{\rm v}$	$\delta_{\rm c}$	z_0	$r_{\rm s}/r_{\rm v}$	σ	A	χ^2
LTB 2014	168^{+15}_{-14}	$-0.13^{+0.05}_{-0.05}$	$0.13^{+0.09}_{-0.05}$	N/A	N/A	N/A	0.98
HSW	190^{+20}_{-30}	-0.5	$0.45^{+0.60}_{-0.13}$	0.9	N/A	N/A	0.99
Multi-voids	5^{+2}_{-0}	-0.92	N/A	0.9	$3.6^{+0.3}_{-0.3}$	$1.75^{+0.25}_{-0.25}$	0.94

5.2 Final Conclusions and Future Prospects

From studying, we find that on large scale the secondary CMB anisotropy is likely to be dominated by ISW effect. The simulations results show that both single void and multiple voids models are well fitting to the CMB cold spot temperature. In this thesis one of our main points is that the single void (especially LTB voids) model is not the unique solution for the origin of CMB cold spot anomaly. The results from LTB, HSW and multiple voids model are equally in term of goodness of fit. The question is what is the most likely to be ?

Firstly, consider LTB (Finelli 2014) model, the Newtonian potential of this model only is Guassian function. If we calculate the ISW effect of this model we will fine that there should not be positive fluctuation (see Figure 3.8). While (Finelli et al., 2014) claimed that their calculation is the RS effect. (Nadathur et al., 2014) had shown that this should be wrong. Recently, Finelli et al. (2015) reconsider their research and find that their model should be fixed. The new model of Finelli et al. (2015) still used LTB geometry embedded in ΛCDM background framework but now the density profile of void is too complicated. The radius of new void model extend from 150 Mpc h^{-1} to 300 Mpc h^{-1}. This new size of void is almost unlikely to be in standard ΛCDM according to void number density theory (see chapter IV, Eq. 4.2 and 4.7).

For single HSW void, We have two concern problems, the big size of void ($r_\mathrm{v} = 190$ Mpc h^{-1}) and the inability of description of the positive temperature fluctuation of cold spot. In fact, we do not expect that the HSW model is well model the large size of void because HSW model is obtained by N-body simulation in ΛCDM framework which only well define small size of voids. We also find that $r_\mathrm{s}/r_\mathrm{v}$ and δ_c of the size of void are also well satisfied the universality of HSW profile. This should be another support evidence of the university of HSW profile. The number density distribution of voids, indicate that super HSW void faces the low probability problem like LTB model. For the problem of positive temperature fluctuation of CMB cold spot, may be only void's ISW effect is not enough. The positive fluctuation should be caused by galaxy cluster. The positive induced temperature of RS (or nonlinear ISW) effect is not unlikely due to large scale of cold spot.

Both single void models require the very big size of void. They face the low probability problem. He can interpret the low probability of existence in four ways. The first way is that just low possibility and the cold spot (super void) just surprising existent structure. Or may be, the void's number density theory is incomplete. Another interpretation is that there must be something that we do not taking to account in standard ΛCDM. The last interpretation is the multiverse model cosmology. May be it is just the coincident of our Universe to has the super void.

For multiple voids model, we try to do realistic simulation as much as possible by put the number density distribution of voids in the simulation. But still we also add special assumption such as the number density of voids in the redshift plane. Now this time, the definition of probability of this event to be real is not well defined. What we learn from the number density of voids in the redshift plane is that σ parameter of normal distribution indicate the interaction range among the voids in redshift plane. The bigger σ mean the stronger interaction of voids in redshift plane.

So far, we had been only considered the CMB cold spot temperature profile. We can not distinguish the origin of cold spot by just consider ISW effect from the single void or multiple voids. We need other observation such as CMB polarisation (Lewis and Challinor, 2006). Because weak lensing of background dependent effect the pattern of CMB polarisation of the single void and multiple voids should be different.

REFERENCES

REFERENCES

Alonso, D., García-Bellido, J., Haugbølle, T., and Vicente, J. (2010). Large scale structure simulations of inhomogeneous Lemaître-Tolman-Bondi void models. **Physical Review D:Particle, Fields, Graviatation & Cosmology** 82(12): 123530.

Alpher, R. A. (1948). A neutron-capture theory of the formation and relative abundance of the elements. **Physics Review** 74: 1577–1589.

Babcock, H. W. (1939). The rotation of the Andromeda Nebula. **Lick Observatory Bulletin** 19: 41–51.

Banday, A. J., Górski, K. M., Bennett, C. L., Hinshaw, G., Kogut, A., Lineweaver, C., Smoot, G. F., and Tenorio, L. (1997). Root Mean Square Anisotropy in the COBE DMR Four-Year Sky Maps. **Astrophysical Journal** 475: 393–398.

Bartelmann, M. and Schneider, P. (2001). Weak gravitational lensing. **Physics Reports** 340: 291–472.

Boggess, N. W., Mather, J. C., Weiss, R., Bennett, C. L., Cheng, E. S., Dwek, E., Gulkis, S., Hauser, M. G., Janssen, M. A., Kelsall, T., Meyer, S. S., Moseley, S. H., Murdock, T. L., Shafer, R. A., Silverberg, R. F., Smoot, G. F., Wilkinson, D. T., and Wright, E. L. (1992). The COBE mission - Its design and performance two years after launch. **Astrophysical Journal** 397: 420–429.

Cai, Y.-C., Cole, S., Jenkins, A., and Frenk, C. (2009). Towards accurate modelling of the integrated Sachs-Wolfe effect: the non-linear contribution. **Monthly Notices of the Royal Astronomical Society** 396: 772–778.

Cai, Y.-C., Cole, S., Jenkins, A., and Frenk, C. S. (2010). Full-sky map of the ISW and Rees-Sciama effect from Gpc simulations. **Monthly Notices of the Royal Astronomical Society** 407: 201–224.

Carroll, S. M., Press, W. H., and Turner, E. L. (1992). The cosmological constant. **Annual Review of Astron and Astrophys** 30: 499–542.

Chantavat, T., Sawangwit, U., Sutter, P. M., and Wandelt, B. D. (2016). Cosmological parameter constraints from CMB lensing with cosmic voids. **Physic Review D** 93(4): 043523.

Cruz, M., Martínez-González, E., Vielva, P., and Cayón, L. (2005). Detection of a non-Gaussian spot in WMAP. **Monthly Notices of the Royal Astronomical Society** 356: 29–40.

Finelli, F., Garcia-Bellido, J., Kovacs, A., Paci, F., and Szapudi, I. (2014). A Supervoid Imprinting the Cold Spot in the Cosmic Microwave Background. **arXiv:1405.1555v2 [astro-ph.CO]**.

Finelli, F., Garcia-Bellido, J., Kovacs, A., Paci, F., and Szapudi, I. (2015). Supervoids in the WISE-2MASS catalogue imprinting Cold Spots in the Cosmic Microwave Background. **Monthly Notices of the Royal Astronomical Society** 455.

Gorski, K. M., Wandelt, B. D., Hansen, F. K., Hivon, E., and Banday, A. J. (1999). The HEALPix Primer. **ArXiv Astrophysics e-prints**.

Guth, A. H. (1981). Inflationary universe: A possible solution to the horizon and flatness problems. **Physical Review D** 23: 347–356.

Hahn, O., Porciani, C., Carollo, C. M., and Dekel, A. (2007). Properties of dark matter haloes in clusters, filaments, sheets and voids. **Monthly Notices of the Royal Astronomical Society** 375: 489–499.

Hamaus, N., Sutter, P. M., and Wandelt, B. D. (2014). Universal Density Profile for Cosmic Voids. **Physical Review Letters** 112(25): 251302.

Hoyle, F. and Vogeley, M. S. (2002). Voids in the Point Source Catalogue Survey and the Updated Zwicky Catalog. **Astrophysical Journal** 566: 641–651.

Hubble, E. (1929). A Relation between Distance and Radial Velocity among Extra-Galactic Nebulae. **Proceedings of the National Academy of Science** 15: 168–173.

Lahav, O. and Liddle, A. R. (2014). The Cosmological Parameters 2014. **arXiv:1401.1389v1 [astro-ph.CO]**.

Lewis, A. and Challinor, A. (2006). Weak gravitational lensing of the CMB. **Physics Reports** 429: 1–65.

Massey, R., Kitching, T., and Richard, J. (2010). The dark matter of gravitational lensing. **Reports on Progress in Physics** 73(8): 086901.

Nadathur, S., Lavinto, M., Hotchkiss, S., and Räsänen, S. (2014). Can a supervoid explain the cold spot? **Physical Review D** 90(10): 103510.

Penzias, A. A. and Wilson, R. W. (1965). A Measurement of Excess Antenna Temperature at 4080 Mc/s. **Astrophysical Journal** 142: 419–421.

Pisani, A., Sutter, P. M., Hamaus, N., Alizadeh, E., Biswas, R., Wandelt, B. D., and Hirata, C. M. (2015). Counting voids to probe dark energy. **Physical Review D** 92(8): 083531.

Planck Collaboration (2014). Planck 2013 results. I. Overview of products and scientific results. **Astronomy** & **Astrophysics** 571: A1.

Planck Collaboration, Adam, R., Ade, P. A. R., Aghanim, N., Akrami, Y., Alves, M. I. R., Arnaud, M., Arroja, F., Aumont, J., Baccigalupi, C., Barreiro, J. J., Bock, A., Bonaldi, L., Bonavera, J. R. Bond, J., Borrill, F. R., and et al. (2015). Planck 2015 results. I. Overview of products and scientific results. **ArXiv e-prints**.

Planck Collaboration, Ade, P. A. R., Aghanim, N., Armitage-Caplan, C., Arnaud, M., Ashdown, M., Atrio-Barandela, F., Aumont, J., Baccigalupi, C., Banday, A. J., Barreiro, R. B., Bartlett, J. G., Bartolo, N. Battoner, E., Benabed, K. Benoı̂t, A., and et al. (2014). Planck 2013 results. XIX. The integrated Sachs-Wolfe effect. **Astronomy and Astrophysics** 571: A19.

Press, W. H., Teukolsky, S. A., Vetterling, W. T., and Flannery, B. P. (2007). *Numerical Recipes 3rd Edition: The Art of Scientific Computing*. Cambridge University Press, New York, NY, USA, 3 edition.

Riess, A. G., Filippenko, A. V., Challis, P., Clocchiatti, A., Diercks, A., Garnavich, P. M., Gilliland, R. L., Hogan, C. J., Jha, S., Kirshner, R. P., Leibundgut, B., Phillips, M. M., Reiss, D., Schmidt, B. P., Schommer, R. A., Smith, R. C., Spyromilio, J., Stubbs, C., Suntzeff, N. B., and Tonry, J. (1998). Observational Evidence from Supernovae for an Accelerating Universe and a Cosmological Constant. **Astronomical Journal** 116: 1009–1038.

Sawangwit, U., Shanks, T., Cannon, R. D., Croom, S. M., Ross, N. P., and Wake, D. A. (2010). Cross-correlating WMAP5 with 1.5 million LRGs: a new test for the ISW effect. **Monthly Notices of the Royal Astronomical Society** 402: 2228–2244.

Sutter, P. M., Lavaux, G., Wandelt, B. D., and Weinberg, D. H. (2012). A Public Void Catalog from the SDSS DR7 Galaxy Redshift Surveys Based on the Watershed Transform. **Astrophysical Journal** 761: 44.

Szapudi, I., Kovács, A., Granett, B. R., Frei, Z., Silk, J., Burgett, W., Cole, S., Draper, P. W., Farrow, D. J., Kaiser, N., Magnier, E. A., Metcalfe, N., Morgan, J. S., Price, P., Tonry, J., and Wainscoat, R. (2014a). Detection of a Supervoid Aligned with the Cold Spot of the Cosmic Microwave Background. **Monthly Notices of the Royal Astronomical Society** 450: 288–294.

Szapudi, I., Kovács, A., Granett, B. R., Frei, Z., Silk, J., Garcia-Bellido, J., Burgett, W., Cole, S., Draper, P. W., Farrow, D. J., Kaiser, N., Magnier, E. A., Metcalfe, N., Morgan, J. S., Price, P., Tonry, J., and Wainscoat, R. (2014b). The Cold Spot in the Cosmic Microwave Background: the Shadow of a Supervoid. **arXiv:1406.3622v1** [**astro-ph.CO**].

Weinberg, S. (1972). *Gravitation and cosmology: principles and applications of the general theory of relativity.* Wiley.

Wu, K. K. S., Lahav, O., and Rees, M. J. (1999). The large-scale smoothness of the Universe. **Nature** 397: 225–230.

APPENDICES

APPENDIX A

1D COLD SPOT ANOMALY TEMPERATURE PROFILE

Table A.1 1D Cold Spot Anomaly Temperature Profile.

$\theta(^\circ)$	$\Delta T(\mu\mathrm{K})$
0.5	-160.29
1.5	-147.27
2.5	-125.42
3.5	-131.43
4.5	-70.05
5.5	-42.40
6.5	-32.98
7.5	-17.97
8.5	-22.38
9.5	-10.01
10.5	3.75
11.5	6.34
12.5	28.93
13.5	44.18
14.5	39.56
15.5	41.04

Continued on next page

Table A.1 – continued from previous page

$\theta(^{\circ})$	$\Delta T(\mu\mathrm{K})$
16.5	34.51
17.5	37.92
18.5	17.19
19.5	24.05
20.5	28.31
21.5	8.66
22.5	3.07
23.5	12.61
24.5	10.98
25.5	6.29
26.5	6.03
27.5	1.32
28.5	4.03
29.5	1.96

APPENDIX B

MORE ON THEORETICAL ISW AND RS EFFECTS

B.1 Perturbed Photon Propagation

Consider the line element in a perturbative metric in spatially flat FLRW spacetime (with conformal time τ),

$$ds^2 = a^2[-(1+2\Psi)d\tau + (1+2\Phi)\delta_{ij}dx^i dx^j], \tag{B.1}$$

where Ψ and Φ are Newtonian potential and curvature perturbation respectively. He define the conformal Hubble quantity $\mathcal{H}$ as,

$$\mathcal{H} \equiv \frac{1}{a}\frac{da}{d\tau} = Ha. \tag{B.2}$$

The photon that propagates through this space still obey the null geodesic and momentum energy relationship

$$k^\mu k_\mu = 0, \tag{B.3}$$

$$\frac{dk^\mu}{d\lambda_s} + \Gamma^\mu_{\alpha\beta}k^\alpha k^\beta = 0, \tag{B.4}$$

where λ_s is an affine parameter and $k^\mu = dx^\mu/d\lambda_s$ is the photon 4-momentum. The solution of these equation will lead us to the propagation of photon definitely. We can simplify Eq. B.4 by split momentum in to background and perturbative form,

$$k^\mu = \hat{k}^\mu + \delta k^\mu. \tag{B.5}$$

At background level, the zeroth component of geodesic equation is

$$\frac{d\hat{k}^0}{d\lambda_s} = -2\mathcal{H}(\hat{k}^0)^2, \tag{B.6}$$

where we have used $\Gamma^0_{00} = \mathcal{H}$ for the flat FLRW metric with the conformal time τ. Integrate above equation, we obtain

$$\hat{k}^0 = \frac{d\tau}{d\lambda_s} \propto a^{-2}. \tag{B.7}$$

This leads to the fact that the frequency redshifts of photon is proportion to 1/a, since $f = dt/d\lambda_s = a d\tau/d\lambda_s$. Perturbing the null-geodesic equation, gives

$$\delta k^\mu \hat{k}_\mu + \hat{k}^\mu \delta k_\mu = 0. \tag{B.8}$$

For radial trajectories the null path condition of photon $ds^2 = 0$ leads to

$$(1+\Psi)d\tau = (1+\Phi)dr, \tag{B.9}$$

or

$$\frac{d\tau}{d\lambda_s} = (1+\Phi-\Psi)\frac{dr}{d\lambda_s}, \tag{B.10}$$

which gives

$$\hat{k}^0 + \delta k^0 = (1+\Phi-\Psi)(\hat{k}^r + \delta k^r). \tag{B.11}$$

We can use the zero-th order equation to obtain $\hat{k}^0 = \hat{k}^r$. The first-order terms give

$$\delta k^0 + \delta k^r + \hat{k}^0(\Phi - \Psi). \tag{B.12}$$

The second order perturbation of Eq. B.4 is ,

$$\frac{dk^0}{d\lambda_s} = -2\mathcal{H}(k^0)^2 - (k^0)^2\left(\frac{\partial\Phi}{\partial\tau} + \frac{\partial\Psi}{\partial\tau} + 2\partial_r\Psi\right) \tag{B.13}$$

Dividing by $k^0 = d\tau/d\lambda_s$, the equation can be rewritten as

$$\frac{1}{a^2k^0}\frac{d(a^2k^0)}{d\tau} = -\left(\frac{\partial\Phi}{\partial\tau} + \frac{\partial\Psi}{\partial\tau} + 2\partial_r\Psi\right). \tag{B.14}$$

From $k^0 = \hat{k}^0 + \delta k^0$ and Eq. B.6, we can refer that

$$\frac{1}{a^2k^0}\frac{d(a^2k^0)}{d\tau} \rightarrow \frac{d(\delta k^0/k^0)}{d\tau}, \tag{B.15}$$

where, at first-oder, we can put equivalently k^0 and $\hat{k}^0$ at the denominator. Now Eq. B.14 becomes

$$\frac{d(\delta k^0/k^0)}{d\tau} = -\left(\frac{\partial\Phi}{\partial\tau} + \frac{\partial\Psi}{\partial\tau} + 2\partial_r\Psi\right). \tag{B.16}$$

B.2 The Sachs-Wolfe effect

Consider Eq. B.16, we realise that there are relation

$$\hat{k}^0\left(\frac{\partial\Psi}{\partial\tau} + \partial_r\Psi\right) = \frac{\partial\Psi}{\partial\tau}\frac{d\tau}{d\lambda_s} + \frac{\partial\Psi}{\partial r}\frac{dr}{d\lambda_s} = \frac{d\Psi}{d\lambda_s} \quad \rightarrow \quad \frac{\partial\Psi}{\partial\tau} + \partial_r\Psi = \frac{d\Psi}{d\tau}. \tag{B.17}$$

Note that, $\hat{k}^0 = d\tau/d\lambda_s$ and $d\tau = dr$ along the unperturbed photon path. Now, Eq. B.16 can be written as

$$\frac{d(\delta k^0/k^0)}{d\tau} = -2\frac{d\Psi}{d\tau} - \left(\frac{\partial\Phi}{\partial\tau} - \frac{\partial\Psi}{\partial\tau}\right). \tag{B.18}$$

Integrating Eq. B.18 leads us to

$$\left.\frac{\delta k^0}{k^0}\right|_E^0 = -2\Psi|_E^0 - \int_E^O \left(\frac{\partial\Phi}{\partial\tau} - \frac{\partial\Psi}{\partial\tau}\right) d\tau, \tag{B.19}$$

where O and E represent the instants of observation and emission, respectively, and $\Psi|_E^O \equiv \Psi_O - \Psi_E$.

The first term is known as the "Sachs-Wolfe" effect and the second term is the ISW effect, the main studying in this thesis. The temperature of a black body distribution of photons is linearity to average frequency $\hat{f}$. Preciously, for a body moving with respect to us with velocity u_μ emit photons with four-momentum k^μ, the temperature of photons which is measure by us is proportional to $-k^\mu u_\mu = \hat{f}$. Hence if a photon is emitted at E and observed at O, the relationship between emission temperature T_E and observed temperature T_0 is

$$\frac{T_O}{T_E} = \frac{(k^\mu u_\mu)_O}{(k^\mu u_\mu)_E}. \tag{B.20}$$

Clearly, the observed temperature fluctuation is

$$\left.\frac{\Delta T}{T}\right|_O = \left.\frac{\Delta T}{T}\right|_E + \left.\frac{\delta(k^\mu u_\mu)}{k^\mu u_\mu}\right|_O - \left.\frac{\delta(k^\mu u_\mu)}{k^\mu u_\mu}\right|_E. \tag{B.21}$$

The four-velocity of the perturbed metric (Eq. B.1) is $u_\mu = [-a(1+\Psi), av_i]$ (Cai et al., 2009). Consider second term of the right hand side of Eq. B.21. The non-zero first-order elements are

$$\frac{k^0 \delta u_0}{k^\mu u_\mu} = \frac{\delta u_\mu}{u_0} = \Psi, \tag{B.22}$$

$$\frac{k^i \delta u_i}{k^\mu u_\mu} = \frac{k^i \delta u_\mu}{k^0 u_0} = -\frac{k^i}{k^0} v_i = e^i v_i, \tag{B.23}$$

where $e^i \equiv -k^i/k^0$ is the basis vector, and the term $(\delta k^0)u_0/(k^\mu u_\mu) = \delta k^0/k^0$ is given in Eq. B.19.

Now, Eq. B.21 becomes

$$\left.\frac{\Delta T}{T}\right|_O = \left.\frac{\Delta T}{T}\right|_E + e^i v_i|_E^O - \Psi|_E^O + \int_E^O \left(\frac{\partial \Phi}{\partial \tau} - \frac{\partial \Psi}{\partial \tau}\right) d\tau. \tag{B.24}$$

The first term is the intrinsic photon fluctuation at the emission event (for CMB it is last scattering surface). The second term represents the Doppler shift. If the Universe have no anisotropic stress (standard ΛCDM), we have $\Psi = -\Phi$. Then the ISW effect will be

$$\frac{\Delta T_{\rm ISW}(\hat{n})}{T} = -2\int \frac{\partial \Phi(\hat{n},\tau)}{\partial \tau} d\tau, \tag{B.25}$$

or in redshift z representation

$$\frac{\Delta T_{\rm ISW}(\hat{n})}{\bar{T}} = -\frac{2}{c^2}\int \frac{\partial}{\partial z}\Phi(z,\hat{n}) dz. \tag{B.26}$$

The potential Φ relate to the matter density fluctuation via Poisson equation,

$$\nabla_\chi^2 \Phi(\hat{n},z) = \frac{3H_0^2}{2}\Omega_m \frac{\delta(\hat{n},z)}{a}. \tag{B.27}$$

In linear perturbation theory, the density fluctuation is related to the linear growth factor by $\delta(\hat{n},z) = D_+(z)\delta(\hat{n},0)$. Therefore, Eq. B.26 and B.27 indicate that,

$$\frac{\Delta T_{\rm ISW}}{\bar{T}} \propto \frac{d}{dz}\left[\frac{D_+(z)}{a}\right]. \tag{B.28}$$

In the case of the flat Universe this would be zero unless the existence of accelerated expansion of the Universe (Λ). So, this make the ISW effect is a good tool to study the dynamic of accelerated expansion of the Universe.

B.3 Angular Power Spectrum of ISW

From Eq. B.25, Expanding the pattern of $\delta_T^{ISW} = \frac{\Delta T_{\rm ISW}}{\bar{T}}$, in terms of spherical harmonics gives,

$$a_{lm} = \int \delta_T^{ISW}(\hat{r}) Y_{lm}^*(\hat{r}) d\hat{r}, \tag{B.29}$$

or in another form

$$a_{lm} = -2\int Y_{lm}^*(\hat{r}) \int \dot{\Phi}(\hat{r},\tau) d\tau d\hat{r}, \tag{B.30}$$

where $\dot{\Phi} = \partial\Phi/\partial\tau$. Writing $\dot{\Phi}$ in terms of a Fourier expansion and using the spherical harmonic expansion of plane wave, $\exp(i\vec{k}\cdot\vec{r}) = 4\pi\Sigma_{lm} i^l j_l(kr) Y^*_{lm}(\hat{k}) Y_{lm}(\hat{r})$ this becomes

$$a_{lm} = -\frac{2}{(2\pi)^3}\int Y^*_{lm}(\hat{r})\int\int \dot{\Phi}(\vec{k},\tau)\exp(i\vec{k}\cdot\vec{r})d\vec{k}d\tau d\hat{r} \tag{B.31}$$

$$= -\frac{2\times 4\pi}{(2\pi)^3}\int Y^*_{lm}(\hat{r})\int\int \dot{\Phi}(\vec{k},\tau)\times \tag{B.32}$$

$$\sum_{l'm'} i^l j_l(kr) Y^*_{l'm'}(\hat{k}) Y_{l'm'}(\hat{r}) d\vec{k}\, d\tau\, d\hat{r} \tag{B.33}$$

$$= -\frac{1}{\pi^2}\int\int \dot{\Phi}(\vec{k},\tau) i^l j_l(kr) Y^*_{lm}(\hat{k}) d\vec{k}\, d\tau. \tag{B.34}$$

The angular power spectrum C_l can be evaluate by

$$C_l\delta_{ll'}\delta_{mm'} = \langle a_{lm} a^*_{l'm'}\rangle \tag{B.35}$$

$$= \frac{1}{\pi^4}\left\langle \int_0^{r_L}\int \dot{\Phi}(\vec{k},r) i^l j_l(kr) Y^*_{lm}(\hat{k}d\vec{k}dr\right. \tag{B.36}$$

$$\left.\times\int_0^{r_L}\int \dot{\Phi}^*(\vec{k}',r') i^{l'} j_l(k'r') Y^*_{l'm'}(\hat{k}') d\vec{k}' d\vec{r}'\right\rangle, \tag{B.37}$$

where r_L indicate that the integration has perform from the present position to the last scattering surface. Using the identity of power spectrum of $\dot{\Phi}$, $\langle\dot{\Phi}(\vec{k})\dot{\Phi}^*(\vec{k}')\rangle \equiv (2\pi)^3\delta(\vec{k}-\vec{k}')P_{\dot{\Phi}\dot{\Phi}}(k)$, and the orthogonality relationship of spherical harmonics

$$\int_{4\pi} Y^*_{lm}(\hat{r}) Y_{l'm'}(\hat{r}) d\hat{r} = \delta_{ll'}\delta_{mm'} \tag{B.38}$$

Eq. B.35 becomes

$$C_l\delta_{ll'}\delta_{mm'} = \frac{8}{\pi}\frac{2}{\pi}\int\int_0^{r_L}\int_0^{r_L} P_{\dot{\Phi}\dot{\Phi}}(k,r,r') i^l j_l(kr) Y^*_{lm}(\hat{k}) \tag{B.39}$$

$$\times\, i^{l'} j_l(kr') Y_{l'm'}(\hat{k}) dr' dr' d\vec{k} \tag{B.40}$$

$$= \frac{8}{\pi}\int\int_0^{r_L}\int_0^{r_L} k^2 P_{\dot{\Phi}\dot{\Phi}}(k,r,r')j_l(kr)j_l(kr')dr'dk\delta_{ll'}\delta_{mm'} \tag{B.41}$$

$$C_l = \frac{8}{\pi}\int\int_0^{r_L}\int_0^{r_L} k^2 P_{\dot{\Phi}\dot{\Phi}}(k,r,r')j_l(kr)j_l(kr')dr'dk. \tag{B.42}$$

For small angular seperations, θ, at comoving distance, r, the wave number, k, can be expressed in terms of its components parallel and perpedicular to the line of sight and approximated by $k = \sqrt{k_\parallel^2 + k_\perp^2} \approx k_\perp$, where $k_\perp = 2\pi/r\theta \approx l/r \gg k\ 1/\Delta r$, namely, the power is dominated by that perpendicular to the line of sight and there is no correlation between different shells of Δr along the line of sight. Using this with the orthogonality relation for spherical Bessel functions, we have

$$\frac{2}{\pi}\int k^2 j_l(kr)j_l(kr')dk = \delta(r-r')/r^2. \tag{B.43}$$

So, the angular power spectrum becomes

$$C_l \approx 4\int_0^{r_L} P_{\dot{\Phi}\dot{\Phi}}(k = \frac{l}{r}, r)/r^2 dr. \tag{B.44}$$

B.4 Rees Sciama Effect

Eq. B.44, we can extend this to nonlinear contribute of ISW effect which is known as Rees-Sciama (RS) effect. In Fourier space, the time derivative of Newtonian potential can be described as:

$$\dot{\Phi}(\vec{k},\tau) = \frac{3}{2}\left(\frac{H_0}{k}\right)^2 \Omega_2 \left[\frac{\dot{a}}{a^2}\delta(\vec{k},\tau) - \frac{\dot{\delta}(\vec{k},\tau)}{a}\right], \tag{B.45}$$

where $\dot{\delta}$ is the time derivative of the density contrast. Applying the continuity equation in Fourier space, $\dot{\delta}(\vec{k},\tau) + i\vec{k}\cdot\vec{p}(\vec{k},\tau) = 0$, to Eq. B.45 gives

$$\dot{\Phi}(\vec{k},\tau) = \frac{3}{2}\left(\frac{H_0}{k}\right)^2 \Omega_2 \left[\frac{\dot{a}}{a^2}\delta(\vec{k},\tau) + \frac{i\vec{k}\cdot\vec{p}(\vec{k},\tau)}{a}\right], \tag{B.46}$$

where $\vec{p}(\vec{k},t) = [1+\delta(\vec{k},\tau)]v(\vec{k},\tau)$ is the momentum density field in Fourier space divided by the mean mass density. The power spectrum, $P_{\dot{\Phi}\dot{\Phi}}(k,\tau) = (2\pi)^{-3}\langle\dot{\Phi}(k,\tau)\dot{\Phi}^{*}(k,\tau)\rangle$, can be evaluate by using Eq B.45:

$$P_{\dot{\Phi}\dot{\Phi}}(k,\tau) = \frac{9}{4}\left(\frac{H_0}{k}\right)^4 \Omega_m^2 \times \left[\left(\frac{\dot{a}}{a^2}\right)^2 P_{\delta\delta}(k,\tau) - 2\frac{\dot{a}}{a^3}P_{\delta\dot{\delta}}(k,\tau) + \frac{1}{a^2}P_{\dot{\delta}\dot{\delta}}(k,\tau)\right]. \quad \text{(B.47)}$$

This is the power spectrum of RS effects (also known as nonlinear ISW effect). While in linear theory $P_{\dot{\delta}\dot{\delta}}(k,\tau) = k^2 P_{vv}(k,\tau) = \dot{D}_+(\tau)^2 P^{lin}_{\delta\delta}(k)$ and $P_{\delta\dot{\delta}}(k,\tau) = kP_{\delta v}(k,\tau) = D_+(\tau)\dot{D}_+(\tau)P^{lin}_{\delta\delta}(k)$, where $P^{lin}_{\delta\delta}$ is the linear density power spectrum at the present time. Therefore, the power spectrum of the linear ISW effect is

$$P^{lin}_{\dot{\Phi}\dot{\Phi}}(k,\tau) = \frac{9}{4}\left(\frac{H_0}{k}\right)^4 \Omega_m^2 \left[\frac{H(t)D_+(t)(1-\beta)}{a}\right]^2 P^{lin}_{\delta\delta}(k), \quad \text{(B.48)}$$

where $\beta = \frac{d\ln D}{d\ln a}$.

CURRICULUM VITAE

NAME: Anut Sangka **GENDER**: Male

NATIONALITY: Thai **DATE OF BIRTH**: September 23, 1990

EDUCATIONS:

- B.Sc. Department of Physics, Ubon Ratchathani University, Thailand, 2013.

PUBLICATIONS

Sangka, A., Sawangwit, U. and Sanguansak, N. 2015, Publication of Korean Astronomical Society, 30, 397-399, **Voids Lensing of the CMB at High Resolution** (Chapters IV)